Circular Solutions

MDS Separation of End-of-Life crystalline PV panels

Circular Solutions

MDS separation of End-of-Life crystalline PV panels

By

S.H.M.I. Alnajar

in partial fulfilment of the requirements for the degree of

Master of Science

in Environmental Engineering

at the Delft University of Technology,

to be defended publicly on Wednesday February 26, 2025 at 13:00 PM.

Supervisor:	Dr. T. Schmiedel	TU Delft
Thesis committee:	Prof. dr. ir. M.W. N. Buxton,	TU Delft
	ir. J.H. Welink,	TU Delft

Contents

Contents

Abstract

The growing volume of end-of-life (EoL) photovoltaic (PV) panels presents a significant challenge and an opportunity for sustainable resource recovery. This thesis investigates the application of Magnetic Density Separation (MDS) to recover and separate valuable non-ferrous metals, such as silicon, copper, zinc, tin, and silver, from crystalline silicon PV waste. The objective of the study is to evaluate the separation efficiency and recovery rates of MDS while addressing economic feasibility and process optimization challenges.

The experimental work involved the use of MDS to fractionate PV waste into light, medium, and heavy-density ranges based on particle size distributions: 200–500 µm, >500 µm–3 mm, and >3 mm–6 mm. X-ray fluorescence (XRF) was employed to analyze the elemental composition of the separated fractions, with leaching processes using hydrochloric acid (HCl) and citric acid applied to assess the purity of magnetic samples. Calibration and instrumental errors, as well as the effects of alloying and particle motion, were accounted for in the analysis. A financial assessment of the MDS process was conducted, examining revenues generated from metal recovery and associated costs, including the economic implications of contamination and refining.

The results revealed that MDS achieved moderate separation efficiencies, with high recovery rates of silica (SiO_2) in the form of glass and sand in the light fractions and silver (Ag) and copper (Cu) in the heavy fractions. However, significant contamination was observed due to overlapping densities of alloyed metals, such as Tin-silver-copper (Sn-Ag-Cu) and Zinc-copper (Zn-Cu), and particle agglomeration during feeding. A financial snapshot demonstrated that medium- and large-sized fractions contributed the most to revenue, driven by silver recovery, with a break-even point requiring the processing of at least 114 tons of PV waste.

In conclusion, MDS shows significant potential as a low-energy, cost-effective solution for recycling EoL PV panels. However, achieving industrial viability requires addressing contamination issues and optimizing the separation process. Future work should focus on integrating complementary refining techniques and scaling up operations to meet purity standards and economic demands. The study also recommends the need for improved ferrofluid magnetization and alloy-specific calibration to enhance detection limits.

Acknowledgements

During my thesis I had help of numerous people and would therefore like to thank them.

I would like to thank my main supervisor Dr. Tobias Schmiedel for his support, input and guiding me through the project. I would also like to thank Stefan Hiller Bernal for having a partner to discuss the topic with and Peter Rem although enjoying retirement proposing this topic to me. Ron Penners, Richard Idzes and the others at Resources & Recycling should also not be forgotten for their great help during the experiments in the lab and their expertise. Finally, special thanks to Jan Henk Welink and Mike Buxton for offering their time to review and advise on this thesis.

1. Introduction

Environmental concern: Energy demand & increasing PV panels becoming waste.

The increasing adoption of photovoltaic (PV) panels, driven by technological advancements, cost reductions, and supportive government policies, has contributed to the growing challenge of managing electronic waste (e-waste). The decommissioning of early PV installations has highlighted the need for effective end-of-life management due to potential environmental risks (Aman et al., 2015). PV panels may contain hazardous substances such as lead (Pb), cadmium (Cd), chromium (Cr), and bismuth (Bi), which can pose health risks. Additionally, the depletion of valuable recoverable materials, including 1 million tons of aluminum, 0.3 million tons of silicon, and 7.4 million tons of glass, along with scarce metals such as silver, indium, gallium, and germanium, is a growing concern (Tao & Yu, 2015; Xu et al., 2018). E-waste generation has steadily increased, with Europe alone reporting a rise from 3.5 million tons in 2010 to over 4.5 million tons in 2016 (Eurostat, 2019). The growing volume of PV installations is expected to further contribute to this issue, with estimates indicating approximately 50,000 tons of PV panel waste generated globally since 2015 (Park & Park, 2014). Future projections suggest that PV panel waste could reach 1.7 million tons by 2030 and exceed 60 million tons by 2050 (Statista, n.d.; IEA, 2020).

Legislation & policy: WEEE directive and the PEACOC Project

The European Union, acknowledging the environmental challenges posed by e-waste, particularly photovoltaic (PV) panels, revised the Waste Electrical and Electronic Equipment (WEEE) Directive in 2012. The revision enforces the Extended Producer Responsibility (EPR) principle, requiring manufacturers to ensure the efficient collection and recycling of PV panels at the end of their life cycle. In addition, the EU has introduced legislative measures to reduce its reliance on non-European raw materials critical for electronic equipment production, including PV panels. The European Raw Materials Initiative, launched in 2008, aims to secure supply chains, enhance resource efficiency, and decrease dependency on imports from regions such as South America, Africa, and China. These efforts contribute to the EU's broader strategy for sustainable growth and resource independence. As part of this initiative, the PEACOC Project was launched in 2021. Within this project, the Resources and Recycling research group at TU Delft focuses on developing cost-effective, energy-efficient methods to recover valuable materials from discarded PV components.

Recycling of PV: Current efforts of recycling PV panels

Material recovery is a key component of the circular economy. A significant challenge in e-waste management is the efficient separation of different materials without degrading their quality, a process known as downcycling (Koffler, 2013). The circular economy concept aims to preserve the value of products and resources by reusing them as secondary components, when they can no longer fulfill their primary function (Pearce & Turner, 1990). However, Waste Electrical and Electronic Equipment (WEEE) presents technical challenges due to the complexity of mixed materials and the wide range of products it encompasses, from mobile phones to refrigerators (OECD, 2001; Puckett et al., 2002).

Current recycling facilities primarily focus on recovering high-value materials such as steel, aluminum, copper, and gold, which are processed into concentrates for sale to smelters or metallurgical refineries (Crowe et al., 2003). However, the decreasing concentrations of these valuable materials in WEEE make their commercial recovery increasingly difficult. Many materials can no longer be concentrated to economically viable levels, highlighting the need for innovative separation methods.

Crystalline silicon modules have historically dominated PV panel production, accounting for over 80% of the market since their early installations in the 1990s (Dambhare et al., 2021). As a result, they represent the largest share of end-of-life (EoL) PV panels requiring treatment. Current recycling methods, primarily based on mechanical shredding and metallurgical processes, are energy-intensive and often result in low recovery rates and material purity (Smith et al., 2018; Jones et al., 2019). Furthermore, pre-treatment techniques such as gravity separation and flotation face limitations due to overlapping material densities and the heterogeneous composition of PV panel residues (Ali et al., 2024). Gravity separation, which relies on differences in specific weight, becomes less effective when materials have similar densities. Whilst flotation techniques struggle with the diverse mixture of materials in PV panels.

These challenges emphasize the need for alternative separation techniques that can simplify material composition before further processing in smelters. This improves recovery efficiency and reduces environmental impact.

Research gap

Magnetic Density Separation (MDS) has demonstrated potential in sorting materials based on density and magnetic properties; however, its application to end-of-life (EoL) photovoltaic (PV) panels remains underexplored. Existing research has primarily focused on bulk material recovery or the extraction of specific elements. Leaving a gap in understanding the efficacy of MDS in isolating non-ferrous metals such as copper, zinc, tin, silicon, lead, and precious metals like silver and gold from the complex mixtures found in PV residues (PEACOC Project, 2021). Additionally, the impact of particle size on separation efficiency and the purity of recovered materials has not been thoroughly investigated. Studies indicate that particle size significantly influences the performance of eddy current separation processes, suggesting that similar considerations are necessary for optimizing MDS applications (Cao et al., 2022). Further research is required to explore the feasibility of MDS in achieving high recovery yields while maintaining economic viability and environmental sustainability.

Objective and goal

With the increasing adoption of PV panels, effective e-waste management and resource utilization are becoming critical. This thesis examines the evolving challenges of PV waste management within the framework of sustainable resource use and circular economy principles. The study focuses on developing an efficient processing route to reduce metallurgical refining costs and promote PV panel recycling. Specifically, this research investigates the application of Magnetic Density Separation (MDS) for recovering non-ferrous metals from end-of-life (EoL) PV panel residues. By analyzing particle size distribution and assessing metal recovery rates and separation efficiencies using X-ray fluorescence (XRF), the study provides valuable insights into the potential of MDS as a sustainable recycling solution. The theoretical framework is presented in Chapter 2, followed by the methodology in Chapter 3, results and discussion in Chapter 4, and conclusions and recommendations in Chapter 5.

Research questions

The findings of this study aim to answer the question:

"Can the application of the Magnetic Density Separation (MDS) based process route establish an effective material separation for the recovery of smaller size (<6mm) non-ferrous metal particles in End of Life (EoL) crystalline (c-Si) PV panels?"

To answer the main question, the problem will be divided into the following sub questions:

- What metals and components are present in EoL (c-Si) PV panels, and how does the MDS process compare to conventional sorting techniques?
- What is the mass distribution of recovered metals across separated fractions, what are their purity levels? how does it affect the economic viability of the MDS process?
- How do different leaching conditions influence the recovery of non-ferrous metals from the ferrous fraction?
- How do XRF instrumental and calibration errors impact the accuracy of metal recovery measurements?

2. Theoretical framework

Types of PV panels

The conversion of light into electricity in photovoltaic or solar cells is rooted in the photovoltaic (PV) effect, consequently, PV panels are primarily classified based on the light-absorbing materials utilized (Tao & Yu, 2015). In broad terms, photovoltaic (PV) modules/panels can be categorized into three main groups: the traditional “1st generation” crystalline silicon (c-Si) wafer-based, the “2nd generation” thin-film and the upcoming “3rd generation” emerging technologies like dye-sensitized and perovskite.

The fundamental unit in solar energy technology is the solar cell. These cells are interconnected and encased within a frame to create a solar module. Multiple modules are then connected to create an array or panel. Figure 1 gives an illustration of this description (Dumbhare et al., 2021).

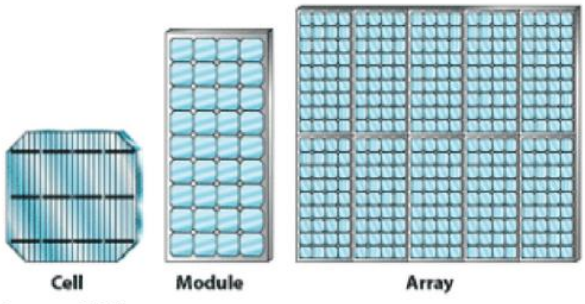

Courtesy of NREL.gov

Figure 1: shows the difference between a solar cell, module(panel) and array.

First “1st” generation solar cells

Solar cells constructed from crystalline silicon wafers are the main focus for the scope of this thesis.

First-generation solar cells are primarily made from crystalline silicon (c-Si), which is the most established and widely used material in the solar industry (Tao & Yu, 2015). These solar cells are typically classified into two types: monocrystalline silicon (Mono-Si) and polycrystalline silicon (Poly-Si). Monocrystalline silicon cells are made from a single continuous crystal structure, offering higher efficiency, usually between 15% and 22%, and longer lifespans, often exceeding 25 years (Deng et al. 2019). However, they are expensive to produce due to the need for high-purity silicon. Polycrystalline silicon cells, on the other hand, are made from silicon crystals melted together. This lowers production costs but also slightly reduces efficiency. First-generation solar cells are known for their high performance in commercial applications, but require significant material use and experience efficiency drops under high temperatures and low light conditions (Tao, J., & Yu, S., 2015) (Dumbhare et al., 2021).

Second “2nd” generation solar cells

Second-generation solar cells, also known as thin-film solar cells, are designed to reduce material use and production costs compared to their crystalline silicon counterparts. These cells are made from a variety of materials, including amorphous silicon (a-Si), cadmium telluride (CdTe), and copper indium gallium selenide (CIGS) (Deng et al. 2019). Thin-film solar cells are much thinner and lighter than first-generation cells, allowing for more versatile applications, such as in building-integrated photovoltaics (BIPV) and portable devices (Dumbhare et al., 2021). They also perform better under low light and high-temperature conditions. However, their efficiency is generally lower, ranging from 10% to 12%, and some types, such as CdTe, involve toxic materials, raising environmental and safety concerns. Additionally, certain thin-film technologies may degrade faster over time, impacting long-term performance (Xu & Zhang, 2018).

Third “3rd” generation solar cells

Third-generation solar cells represent a diverse and emerging class of photovoltaic technologies that seek to overcome the limitations of earlier generations (Xu & Zhang, 2018). These include dye-sensitized solar cells (DSSCs), organic photovoltaics (OPVs), perovskite solar cells, and quantum dot solar cells (Deng et al. 2019). Many of these technologies use novel materials and designs to potentially achieve higher efficiencies at lower costs. For example, perovskite solar cells have shown remarkable efficiency improvements in laboratory settings, with some reaching over 25% (Frischknecht et al., 2020). Moreover, third-generation solar cells can be flexible, lightweight, and even transparent. Making them suitable for a wide range of new applications, including wearable devices and solar windows (Dumbhare et al., 2021). Despite their promise, these technologies face challenges with stability, durability, and environmental impact, and are still in the research and development phase with limited commercial availability.

Components and material composition of crystalline silicon (c- Si) PV panels

A standard panel is composed of an aluminum (Al) alloy frame, hardened glass, a piece of battery (lead acid), EVA (an ethylene/vinyl acetate copolymer), and a backboard/substrate (TPT, Topotecan Hydrochloride) See figure 2.

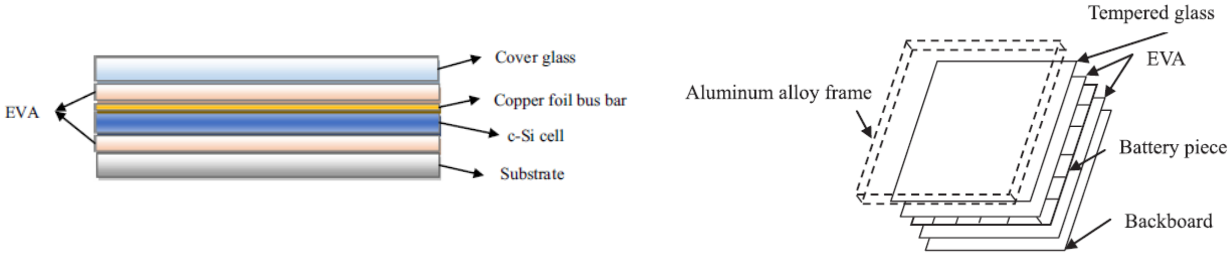

Figure 2: on the right shows the common structure of components in a solar panel while on the (left) shows the illustration of a c-Si solar panel (Yin and Hao, 2009) (Xu, Y., et al. 2018).

The solar cells and interconnecting ribbons form a thin layer, which, while only making up about 5% of the total weight, contribute to over half of the value (as shown in Table 1). The base of a solar cell is a silicon wafer of extremely high purity, typically surpassing 99.9999% purity, and accounting for 4.4% of the weight. Electrical contacts are established by screen printing silver (0.03% weight) and aluminium (0.3% weight) onto the surface. The interconnecting ribbon primarily consists of copper (0.8% weight), with a coating of tin (0.1% weight) and lead (0.01% weight). The front glass sheet and backsheet, which contain PVF (polyvinyl fluoride) and PET (Polyethylene terephthalate), serve as protective layers, akin to two slices of "bread". This is important for safeguarding the solar cells from physical damage throughout their 25-year operational lifespan (Tao, J., & Yu, S. 2015). Some models substitute the polymer back sheet with glass. These various layers are encapsulated by EVA (ethylene-vinyl acetate) under specific temperature and pressure conditions. This encapsulated structure is then affixed to an aluminium frame (16% weight) using silicone, providing protection to the internal components from thermal and mechanical stress (Deng et al., 2019, Domínguez and Geyer, 2019, Frischknecht et al., 2020).

Table 1: Weight and value composition of a first-generation typical crystalline silicon photovoltaic module (Deng and Zhuo 2022).

Material	**Weight in %**	**Unit price ($/kg)**	**Recycled revenue ($/m²)**
Solar cell			
Silicon	4.4	2.7	1.30
Aluminum	0.3	1.5	0.05
Silver	0.03	647	1.79
Ribbon			
Copper	0.8	4.4	0.38
Tin	0.1	16	0.18
Lead	0.01	2	0.00
Glass (solar glass)	67	0.091	0.67
Plastics			
EVA	6.7	Waste to energy*	0.14
PVF	0.8		
PET	2.6		
Silicone	0.9		
Frame	16	1.5	2.7
Aluminum			
Total	99.64	675.191	5

* The most common practice is waste to energy, with recycled revenue of $0.14/m2.

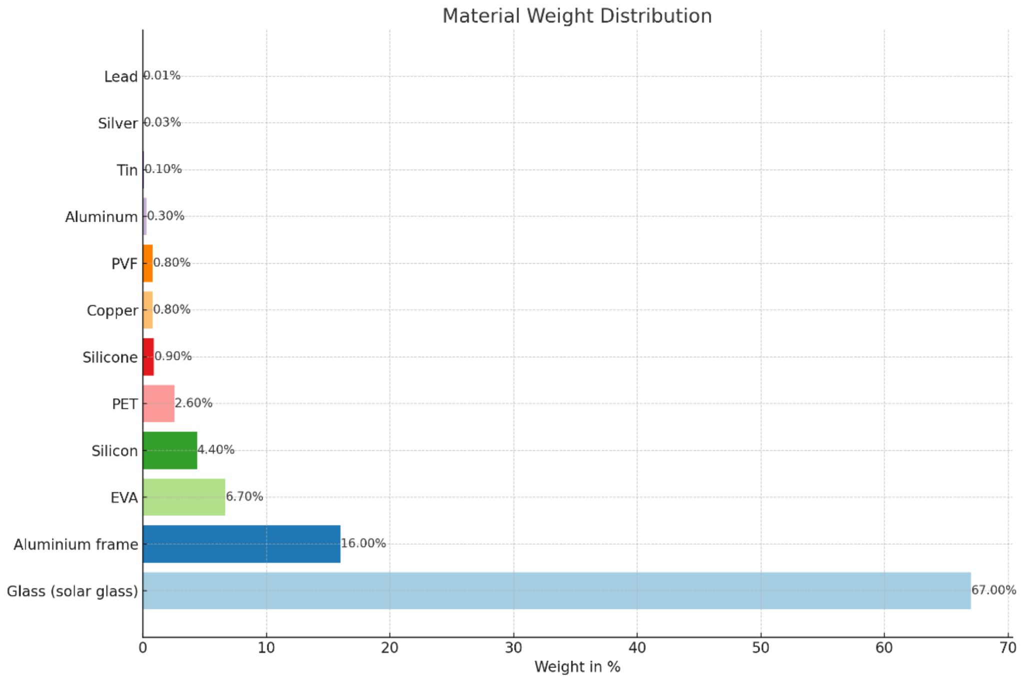

Figure 3: material weight distribution in percentage from the numbers used table 1.

Material mixing and Separation

In the context of sustainable resource management, recycling plays a crucial role in mitigating environmental impact. The recycling of complex products, such as solar panels, involves intricate material compositions and poses challenges related to material mixing and separation. To address these issues, Dahmus and Gutowski, developed an information theory-based model for product recycling. This model departs from traditional approaches, such as the Sherwood Plot.

The Sherwood Plot and Its Role in Recycling

The Sherwood Plot, originally developed to analyze the cost of purifying materials from dilute solutions, is a well-established tool used in material recovery and recycling. It demonstrates the relationship between the concentration of a material in a mixture and the energy or cost required to extract and purify it. In essence, the plot shows that as the concentration of a valuable material decreases, the cost of recovering it increases exponentially. This concept is particularly relevant in the recycling of complex products, where materials are often present in small quantities and are mixed with other components.

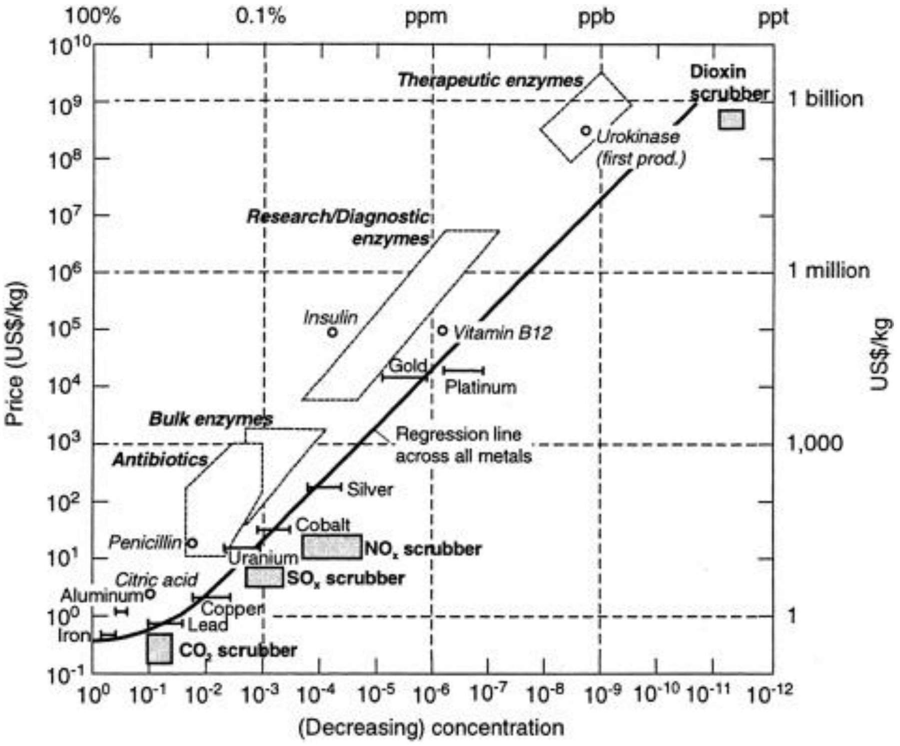

Figure 4: shows the sherwood plot and the relationship of the material concentration (x-axis) representing how diluted or dispersed a material is within a product and the separation cost (y-axis) showing the financial or energy cost required to recover the material at different concentrations (Dahmus and Gutowski, 2007).

Application to Recycling

In recycling, the Sherwood Plot (figure 4) highlights a key challenge: high-value materials, such as silver in solar panels, are often present in low concentrations, making their recovery costly and resource-intensive. For example, recycling an aluminum can, where aluminum is the dominant material, is relatively straightforward and cost-effective. However, extracting silver from solar panels, where it exists in small amounts and is intertwined with other materials, requires more complex and expensive separation processes.

Limitations of the Sherwood Plot

While the Sherwood Plot provides valuable insights into recycling economics, it has limitations when applied to complex, multi-material products like solar panels. The traditional plot primarily considers individual materials rather than the interactions and entanglements of multiple materials within a product. This is where Dahmus and Gutowski's model offers an improvement by incorporating information theory to account for the complexity of material separation.

Dahmus and Gutowski's Model:

The model evaluates the feasibility of recycling by quantifying the "information content" of a product's material composition. In essence, it estimates how difficult it is to separate the materials based on how mixed or dispersed they are within the product. The more mixed the materials, the higher the "information entropy," requiring more effort and cost to achieve separation.

The key equation used in the model is:

$$\sum_{i=1}^{M} \mathrm{m}_i k_i > H k_b \quad (2.1)$$

Where:

- $m_i = mass\ of\ material\ i\ (kg)$,
- $k_i = economic\ value\ of\ material\ i\ (\$\ per\ kg)$,
- $k_b = processing\ cost\ per\ bit\ (\$\ per\ bit)$,
- $H = measure\ of\ material\ mixing\ (bits)$,
- $M = number\ of\ materials\ in\ the\ product.$

The term H derived from Shannon's entropy equation, represents the complexity of material separation, reflecting the number of steps required to isolate a specific material from the mixture. The higher the value of H, the more difficult and costly the recycling process becomes.

The entropy H is calculated as:

$$H = -\sum_{i=1}^{M} c_i log_2 c_i \quad (2.2)$$

Where:

- $M = number\ of\ materials\ in\ the\ product,$
- $c_i = concentration\ of\ material\ i$

This formula quantifies the level of mixing by considering the distribution of different materials within the product.

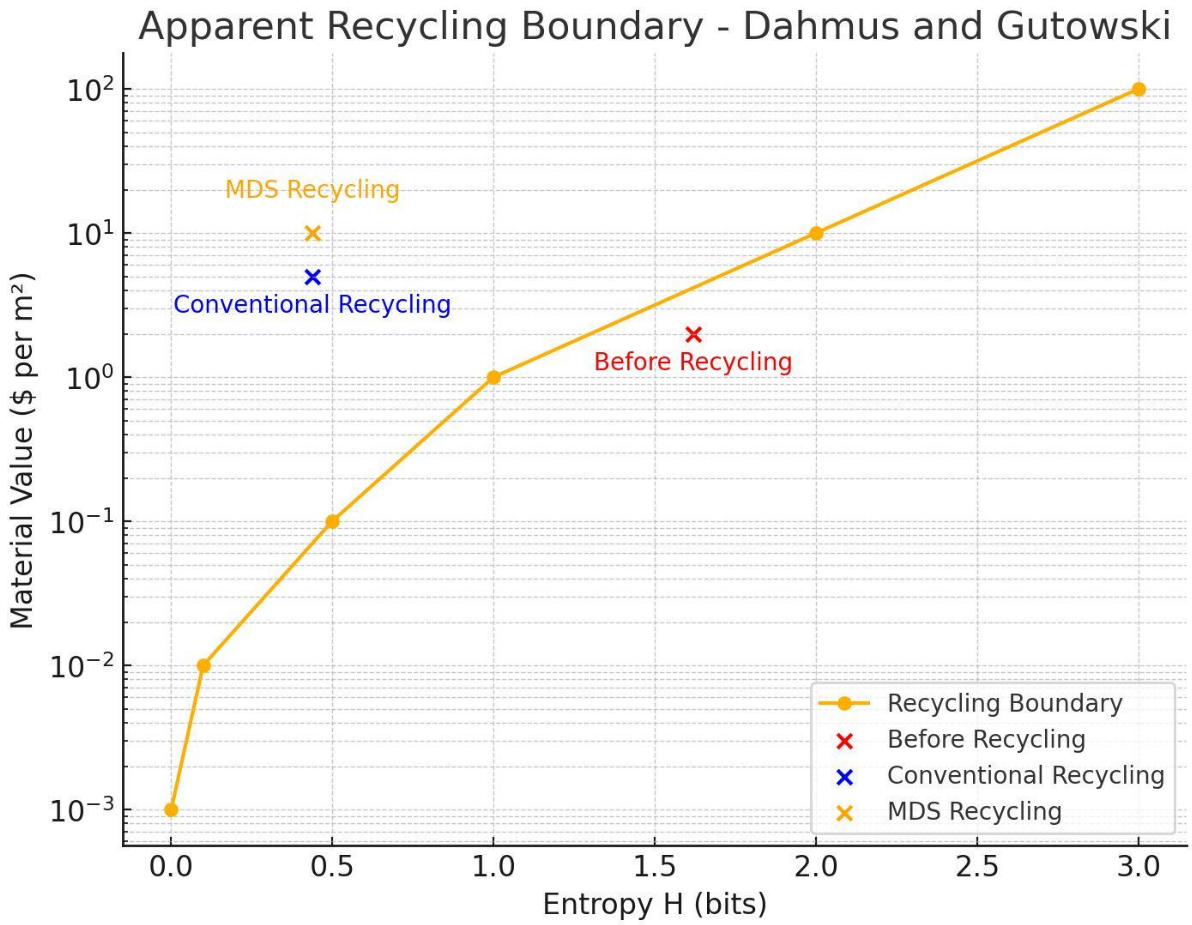

Figure 5: shows the "apparent recycling boundary" calculated using the Dahmus and Gutowski model and the estimated positions of the entropy value H before recycling, conventional recycling and recycling with MDS against its recycled revenue material value in dollar per m^2 of a crystalline solar panel according to their compositions in table 1.

Figure 5 displays the material value (in dollars per m^2) on the y-axis and the degree of material mixing (Entropy, H), measured in bits on the x-axis calculated with equation 2.2. The boundary represents the practical limitations of recycling processes, where a crystalline PV panel positioned below the curve without being recycled reflects a high entropy value H of 1.62 bits assuming just the removal of the aluminum frame would achieve a total revenue of approximately 2 \$/m^2. The high entropy value also indicates the challenge to recycle efficiently due to high separation costs relative to its material value. However, conventional recycling methods such as mechanical and chemical processes have managed to separate valuable components such as silver and copper, from the lower value materials like glass and silicon. Assuming a separation efficiency of 95% can achieve a total recycled revenue of 5 $\$/m^2$ (Deng and Zhou, 2022) and a calculated entropy H of 0.324. With magnetic density separation the entropy value is predicted to remain unchanged reflecting some improvement in material separation but ideally improve the total revenue value up to 10 $\$/m^2$ or higher. The graph highlights the economic potential of MDS recycling, showing that it might increase the value of recovered materials compared to conventional methods. The next chapter will go more into depth on some of the current recycling technologies for c-Si PV panels and their ability to separate different material groups.

3. Conventional recycling technologies for c – Si PV panels

The process of recycling crystalline silicon modules typically involves two primary stages: the removal of the encapsulant from the laminated assembly and the extraction of metal from the silicon cells (Deng et al., 2022). The intermediary step of material sorting connects these critical phases, facilitating a process that is both efficient and productive. Once the materials are delaminated, they are categorized into groups according to various physical attributes, including density, flexibility, light transmission ability, and electrostatic properties. Figure 6 illustrates the operation of diverse material sorting techniques.

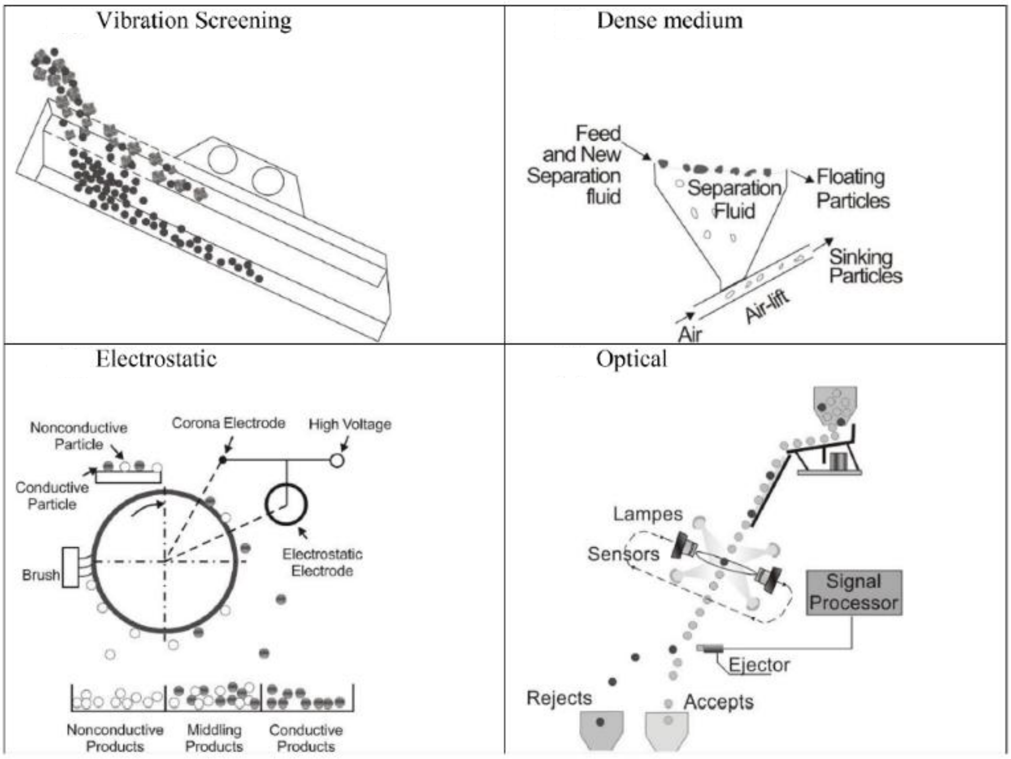

Figure 6: Schematics of mainstream material separation technologies in current recycling of c-Si pv panels (Deng and Zhuo 2022).

Vibratory screening is employed to sort various fractions by their size, often in conjunction with mechanical breakdown. The largest fraction, typically exceeding 5 mm in diameter, predominantly consists of backsheet polymers and copper ribbons. These materials exhibit greater elasticity and flexibility, making them less susceptible to crushing forces. This fraction also includes glass, silicon, and silver, which remain partially laminated and not fully detached (Azeumo et al., 2019; Del Pero et al., 2019). The intermediate fraction, ranging from 0.4 to 5 mm, often comprises directly recyclable glass; for instance, one study revealed that the 0.4–1 mm fraction contains 18% by weight of such glass (Pagnanelli et al., 2019).

Density separation techniques, also known as dense medium or gravimetric separation, classify materials based on their mass-to-volume ratio. This separation typically occurs in a fluid with an intermediate density, so that the feeding material will either float or sink (Savvilotidou and Gidarakos, 2020; Song et al., 2020). Song et al. shows in his study that, heavy liquids with a density of $2.4\ g/cm^3$ have been used to separate glass $2.5\ x\ 10^3\ kg/m^3$ and silicon powder $2.3\ x\ 10^3\ kg/m^3$ based on their respective densities for 300-500 µm sieved product fraction. Another liquid with a density of $3.0\ x\ 10^3\ kg/m^3$ concentrated silver $10.5\ x\ 10^3\ kg/m^3$ and removed glass $2.5\ x\ 10^3\ kg/m^3$and silicon powder $2.3\ x\ 10^3\ kg/m^3$ for smaller product fractions (less than 20μm) (Song et al. 2020).

Optical sorting mechanisms can identify and remove impurities that differ in color from the desired cullet. In the context of module recycling, fragments of solar cells can be detected and ejected using compressed air (Wambach, 2017). Notably, several European photovoltaic recycling plants have implemented optical sorting to reclaim white glass cullet from discarded modules ("PVCycle France," 2021; Wambach, 2017). Optical sorters enhance the purity of the recycled material by removing colored impurities, contributing to the efficiency of module recycling.

Electrostatic separation, which differentiates materials based on electrical conductivity, involves passing substances through a grounded roller and subjecting them to electric charge ionization from an electrode. Conductive particles are charged due to physical contact with the roller and non-conductive particles are attracted to the roller due to Coulomb forces (Zhang et al., 2017). Research has demonstrated that up to 95% by weight of metal fractions can be isolated into conductive groups, effectively separating them from non-conductive materials like glass and polymer (Dias et al., 2018b).

Although these mechanical sorting techniques have proven to be effective, they are often limited to targeting one or two materials per technique. Manual sorting, although effective, is labor-intensive and unsuitable for high-volume processing. For example, chemical delamination using toluene immersion necessitates manual removal of the glass, backsheet, and cells with tools such as files and tweezers. Similarly, a process involving heating modules to soften the encapsulant (EVA) and manually separating the components has been reported, but it demands significant labor input (Dias et al., 2021b; Riech et al. 2021). Lastly, the exposure to lead which can be inhaled or digested can lead to serious health risks including cognitive impairments, cardiovascular problems and reproductive toxicity (Schileo & Grancini, 2021).

Magnetic Fluid (Ferrofluid) as a separation medium

Magnetic fluids, also known as ferrofluids, are a unique class of colloidal liquids that contain nanoscale ferromagnetic or ferrimagnetic particles suspended in a carrier fluid, such as water or oil. These magnetic nanoparticles, typically iron oxide (Fe_3O_4), are coated with surfactants to prevent agglomeration and ensure stable dispersion within the fluid. Ferrofluids exhibit superparamagnetic properties, which means they can be magnetized under an external magnetic field and lose their magnetization when the field is removed. This dynamic behavior makes them highly versatile in various applications, particularly in separation technologies (Odenbach, 2003; Raj & Moskowitz, 1990). In this study, ferrofluids are employed as the separation medium to analyze three distinct particle size ranges. The magnetic properties of the fluid enable efficient and accurate segragation of particles based on their density, enhancing the overall resolution of the separation process. Compared to traditional separation media, ferrofluids provide superior control and flexibility, making them a crucial component of the MDS process applied in this research (Van Silfhout et al., 2013).

The use of ferrofluids as a separation medium is primarily based on the magneto-Archimedes principle. This leverages the balance of gravitational and magnetic forces on particles within the fluid. In the presence of a non-uniform magnetic field, particles with different densities and magnetic susceptibilities experience different magnetic buoyancy forces, allowing for their separation.

Novel sorting technique: MDS (Magnetic Density Separation)

Magnetic Density Separation (MDS), a technology developed in 2005 by the Resources and Recycling group at Delft University, offers an innovative approach to achieving finer separation of materials based on density (Bakker et al., 2010; Resources & Recycling, 2013). The key advantage of MDS is its ability to separate materials with varying densities in a single process, efficiently distinguishing between light and heavy particle concentrations. The technology is capable of handling materials with densities ranging from $0.8\ \mathrm{x}10^3$ up to $20\ \mathrm{x}10^3$ kg/m^3 (Hu et al, 2011)(Wang, 2014) (Bakker, Rem, & Fraunholcz, 2009).

Applications of MDS in WEEE

Wang et al. (2024), developed an innovative MDS process for sorting granular solid wastes, including shredded printed circuit board assemblies (PCBA's) and wires. Their experiments demonstrated the role of MDS in concentrating valuable metals and reducing metallic contaminants in plastic fractions. Similarly, Van Beek et al. (2023). reported that MDS could separate parts by density, effectively isolating heavy metal components from lighter plastics in electronic waste. Their process achieved a concentration increase by a factor of 6,4 enhancing the purity of recovered materials.

While MDS has proven effective for electronic waste and other mixed material streams, its application to end-of-life PV panels remains underexplored. This study seeks to bridge this gap by evaluating the potential of MDS to recover non-ferrous metals and silicon from PV residues in a single step, providing a sustainable alternative to conventional multi-step recycling processes.

Principle

The principle of the MDS uses a ferro(magnetic)-fluid as a separation medium in a magnetic field. Usually water based, the density of the magnetic fluid varies with the distance from the magnet in a special magnetic field (Hu, 2014). Such liquid contains particles of magnetic iron oxide with a size of approximately 10-20 nm suspended in water. The apparent liquid density (equation 3.1) in a magnetic field increases as the magnet attracts the magnetic nano-particles.

$$\rho_{apparent} = \rho_{liquid} + \frac{2\pi M B_o}{g w} e^{-2\pi z/w} \quad (3.1)$$

Where ρ_{liquid} is the density of the liquid, M the magnetization of the magnetic field, B_o the magnetic induction of the magnet at (z=0), w the wavelength of the magnetic field, z the vertical distance from the magnet and g gravitational acceleration (9.81 m/s^2). The particles in the magnetic liquid take some time to reach the height of equilibrium where their density is the same as the apparent liquid density. The processing time is a function of particle terminal velocity which changes due to the exponential gradient of the apparent density.

The term $\frac{2\pi M B_o}{g w} e^{-2\pi z/w}$ represents the contribution of the magnetic field to the apparent density. This term shows that the apparent density decreases exponentially with distance z parallel to the magnet plane. The exponential term $e^{-2\pi z/w}$ indicates that as you move further from the reference point (in the direction of z), the influence of the magnetic field on the apparent density decreases. This creates a gradient where the apparent density is higher when closer to the magnet and decreases as you move away.

When a magnet is placed beneath a magnetic fluid, it exerts a downward magnetic attraction on the fluid. This interaction results in an upward force called "fluid magnetic buoyancy" acting on non-magnetic particles within the fluid. Interestingly, particles with densities higher than that of the fluid can float instead of sinking. As these particles move downward toward the magnet, the fluid magnetic buoyancy continues to increase. Consequently, when a particle is dropped into the fluid, it neither sinks to the bottom nor floats at the surface. Instead, it suspends at a specific height where the combined effect of fluid magnetic buoyancy and the original buoyancy (without a magnetic field) balances gravity.

When a particle moves through the fluid along its inclined trajectory reaches the horizontal bottom of the basin, it slides forward instead of stopping immediately. This phenomenon, known as particle sliding has been studied on granular solid wastes (Wang et al., 2024). Terminal velocity (equation 3.2), refers to the maximum constant velocity when the forces acting on it, gravitational, buoyant, and drag are balanced, influencing the processing time of the separation process. Terminal velocity changes due to the exponential gradient of the apparent density of the medium. This means that the terminal velocity increases with a greater density difference between the particle and the fluid and is influenced by the particle's shape and size.

$$v = \sqrt{\frac{2(\rho_p - \rho_{app})Vg}{C\rho_{app}A}} \quad (3.2)$$

Where g is the acceleration of gravity, ρ_p is the density of the particle, V and A are the volume and the cross-section area of the particle and C is the coefficient of drag which is a function of the shape of the particle (Bakker et al, 2010).

Analysis of materials by XRF spectrometer

In this study, X-ray Fluorescence (XRF) was chosen as an indicative method to characterize the metals recovered from the MDS process due to its broad detection capabilities and suitability for preliminary analysis. XRF can simultaneously detect and quantify elements from sodium (Na) to uranium (U) without prior knowledge of the sample composition, making it ideal for providing an overview of the metallic content (Jenkins et al., 1995). It is a rapid, non-destructive technique commonly used in various applications, including the analysis of platinum group metals (PGM) concentrates (Yoon et al., 2005), precious metal (PM)-containing ceramics (Tsolakidou & Kilikoglou, 2002), alloys (Zwicky & Lienemann, 2004), and rare earth elements from ashes (Smoliński et al., 2016). Additionally, XRF can measure the thickness and composition of different layers and coatings (Brouwer, 2006). While it provides qualitative and semi-quantitative data rather than the high precision of techniques like ICP-MS, it offers a reliable estimate of elemental concentrations. This information is sufficient to assess the general composition of the recovered metals and evaluate the effectiveness of the MDS process in concentrating specific elements (Willis et al., 2014).

Principle of XRF

A source, typically an X-ray tube, generates X-rays that irradiate the sample. This causes the elements in the sample to emit fluorescent X-ray radiation. These emissions have distinct energy levels, akin to different colors in visible light, which are unique to each element. By identifying these energy levels (or "colors"), we can discern the elements present in the sample. Additionally, by assessing the intensity of these energy emissions (or "colors"), we can estimate the quantity of each element in the sample (Brouwer, 2006).

The Bohr model in atomic physics presents an atom as a tiny nucleus carrying a positive charge, with electrons orbiting around it. These electrons are drawn towards the nucleus by electrostatic forces. When X-ray radiation, such as that from X-ray tubes, hits matter and its energy is sufficiently high, specifically surpassing the bond energy of the electrons in their orbitals (ionization energy), it triggers the emission of electrons via the photoelectric effect. In the photoelectric effect, electrons absorb energy from photons and are then ejected from the matter, resulting in the destruction of the photon. The energy absorbed is equivalent to the bond energy of the ejected electron. The residual energy, calculated as, $E_{kin,\,Photo\text{–}electron}=E_{Photon}–E_{Binding}$, is carried by the ejected photo-electron.

This process can only occur if the energy of the incident radiation exceeds the electron's ionization energy. This leads to the creation of vacancies on the orbitals, resulting in the ionization of the atom. These vacancies are filled by an electron transition from an outer orbital, allowing the atom to relax. As the bond energy of outer orbital electrons is always greater than that of inner ones, energy is released during the electron transition. This energy can be emitted as secondary fluorescence radiation, although it competes with the Auger effect. This secondary X-ray radiation is unique to each element and each individual electron transition (Weiss, 2012). Figure 6 shows an illustration of the physical principle of the XRF fluorescence.

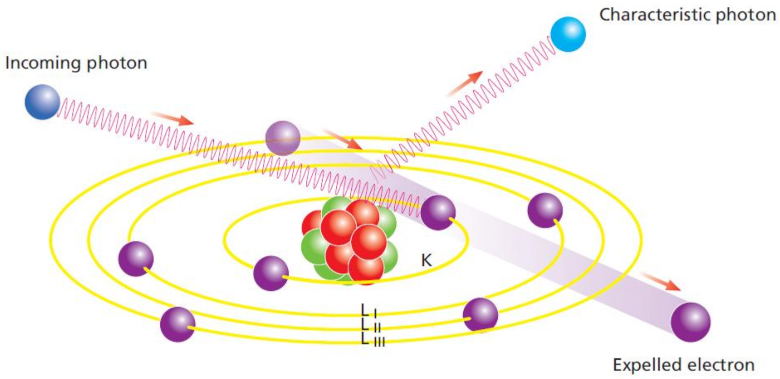

Figure 6: Production of characteristic radiation (Brouwer, 2006).

By measuring this radiation with specific detectors in this case a spectrometer, it's possible to identify the elemental composition of the targeted material. The disadvantage of a spectrometer is that it only analyzes the sample’s surface layer, so it must be representative of the whole sample.

Measuring Recovery

In the context of PV panels, "recovery" refers to the process of extracting valuable metals from end-of-life PV panels. This process is a crucial part of the recycling and end-of-life management of PV modules. It involves the extraction of metals such as silicon, silver, aluminum, and others from PV panels that have reached the end of their operational life (Theocharis et al., 2022). Measuring the recovery of metals from PV panels involves assessing the efficiency and effectiveness of the extraction processes. This includes the evaluation of the amount of each metal recovered, the purity of the recovered metals, and their environmental impact of these processes (Abdo & El-Shazly, 2023).

4. Methodology

This study combines Magnetic Density Separation (MDS) and X-ray Fluorescence (XRF) analysis to characterize the metallic composition of samples with initially unknown properties. The MDS process is utilized to separate particles based on their density differences with the help of a ferrofluid, enabling an effective segregation of various metallic fractions. This separation technique will be used to concentrate the non-ferrous metals; Silica (Si), Zinc (Zn), Tin (Sn), Copper (Cu) and Silver (Ag) within the sample. Following MDS separation, XRF analysis is conducted to provide a preliminary identification and quantification of the elemental composition of the separated fractions. XRF is chosen for its non-destructive nature, rapid analysis capability, and ability to detect a wide range of elements, making it an ideal tool for characterizing the metallic content of the samples. The combined use of MDS and XRF allows for a comprehensive assessment of the sample composition, ensuring accurate and efficient evaluation of the materials under study.

4.1. Materials and Equipment

0-3 mm sample

The first fraction of ca. 50 kg the wet 0-3 mm non-ferrous metal residue was received from Comet group, in Belgium. The fraction was sieved wet at 500 µm, 200 µm and 63 µm and the grainsize distribution investigated (see figure 7). A large portion of the fraction especially the (63–200 µm fraction) consisted of sand (silica). Therefore, it was decided to dry the size fractions and separate each size fraction over a rotary drum magnet first before removing the sand fraction with a hydro cyclone. For the 0–63-µm fraction and the 63–200 µm fraction was decided to not further process it with MDS as very fine particle sizes tend to consume a large amount of ferrofluid and would be difficult to recover.

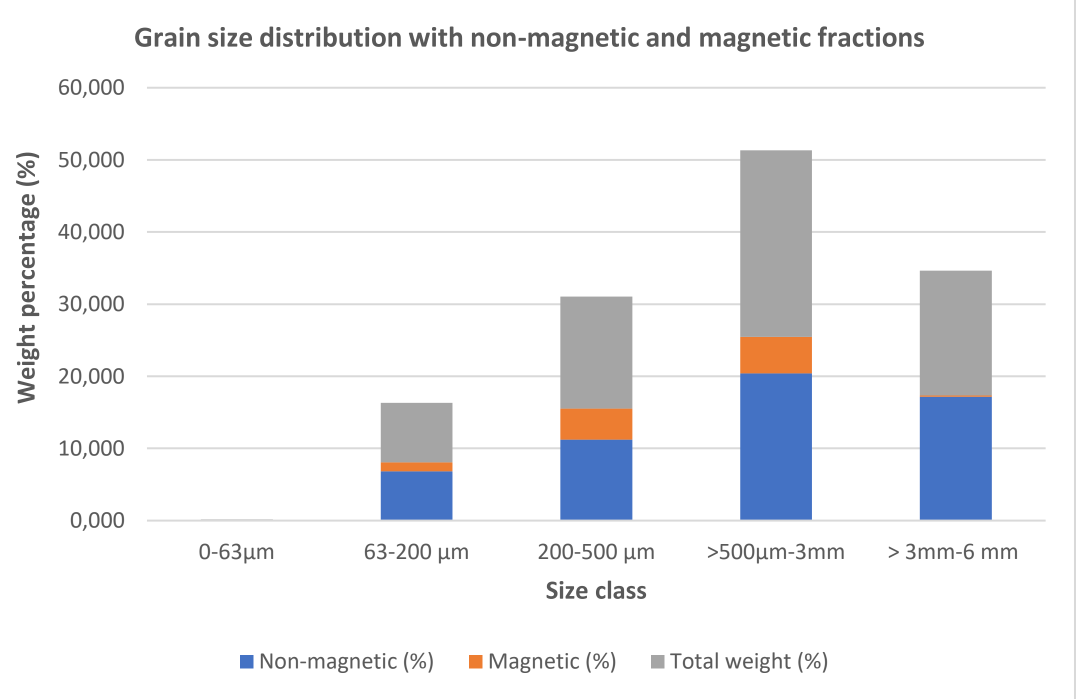

Figure 7: shows the grain size distribution of the 0- 3 mm fraction and the > 3mm samples.

>3 mm sample

The second fraction of ca. 50 kg wet >3 mm non-ferrous metal residue was also received from Comet group, Belgium. The sample was sieved dry at 3mm and 6 mm. The fraction larger than 6 mm was not investigated as it was out of the scope of this study. Since this sample consisted of very little fines, only magnetic separation was applied before processing it with MDS.

Considering the scope of the research it has been decided to analyze the separation of the following five target non-ferrous metals and their densities:

Metal	***Density (ρ) kg/m3***
Silicon (Si)	2.330
Silica (SiO2)	2.650
Zinc (Zn)	7.068
Tin (Sn)	7.260
Copper (Cu)	8.944
Silver (Ag)	10.497

Tabel 2: shows the density of the metals in solid form at room temperature.

Figure 8: shows the lab setup for the experiment of the MDS process.

A three gutter (68 x 11 x 9 cm each) plastic container was created (see figure 8). A permanent magnet and a pump for the injection of the ferrofluid.

The leveled container is positioned on an angled magnet (9°) with a surface magnetic field of 0.6 T and a wavelength of 0.12 m. The container was placed 10 cm from the beginning of the magnet for a more stable magnetic field from the magnet. All components are introduced into the liquid at the same location (left side of figure 8). Lastly, two magnetic fluid dilutions were investigated, with a density of 1.058 kg/m^3 and a magnetization of 12.000 A/M. The magnetic fluid used was a diluted magnetite ferrofluid (1:3) produced by Ferrotech. This ferrofluid dilution was used for the larger particle sizes of 500 µm -3 mm and bigger than 3 mm. For the finer particle sample of 200-500 µm the dilution was chosen to be at (1:5) as finer particles tend to consume more ferrofluid because of its stickiness.

XRF

The XRF used for the analysis of the samples was the PANalytical Epsilon 3 XLE Fluorescence (EDXRF) Spectroscopy system. This Epsilon 3XL is equipped with the silicon-drift detector technology. Pulse-reset electronics give a count rate capacity of over 200 000 cps and a count rate independent resolution, typically better than 135 eV. An exclusive deconvolution algorithm with automatic line-overlap and matrix corrections, advanced environmental fundamental parameter control and condition optimizer provides reliable results for many different types of materials. Key specifications and options for the system is presented in table 3.

Parameters	***Type***	***Measurement***
X-ray tube	Ceramic	50 µm
Anode material	Rhodium (Rh)	
Tube settings	Software controlled	Max.voltage 50 kV, max. current 3.0 mA
Tube filters	Cu 300 µm, Al 50 µm, Al 200 µm, Ag 300 µm, Cu 500 µm, Ti 7 µm	
Detector	High resolution Si drift (SDD)	Resolution typically 135 eV at 5.9 keV/1000 cps
Purge	Helium	Energy < 3 keV

Table 3: shows key specifications of the PANalytical Epsilon 3 XLE Fluorescence (EDXRF) Spectroscopy system.

4.2. Experimental procedure

The gutters were filled to the same level (6.3 cm deep) with ferrofluid by using a pump, this was always measured on the right side of the setup as less ferrofluid would accumulate due to the magnet. The feed with non-ferrous metal particles were first wetted with ferrofluid to reduce the effect of air bubbles playing a role in altering particle density. After that, to allow suspension of particles to their equilibrium heights and avoid as much particle-to-particle interaction for best possible separation, the particles were slowly fed with a shaker (see figure 8) to consistently drop from a height of 11.5 cm (above the bottom of the container).

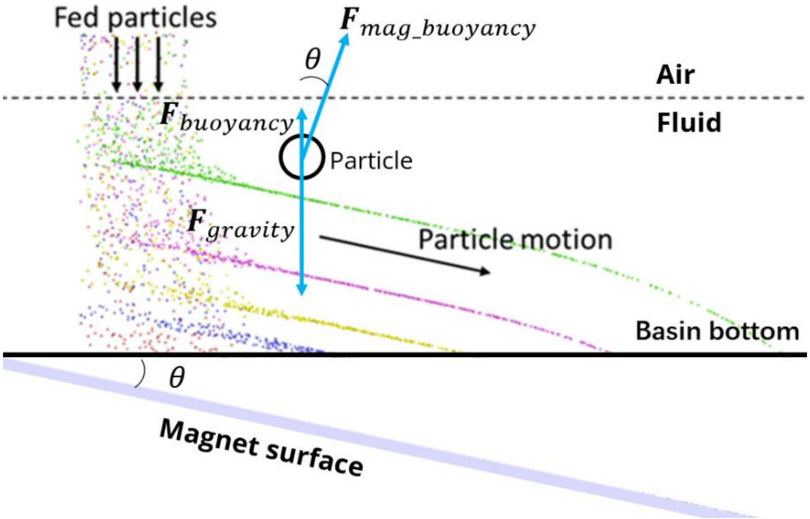

Figure 9: shows an illustration of the forces on the particles with different densities fed into the container with ferro-fluid. (Wang et al., 2024)

After all the feedstock is placed into the liquid at the same position the particles will slowly move to the right settling at their equilibrium positions according to their effective densities. Therefore, separated by density over the length of the box (See figure 9). Unfortunately, only one experimental run was performed, due to time and setup limitations.

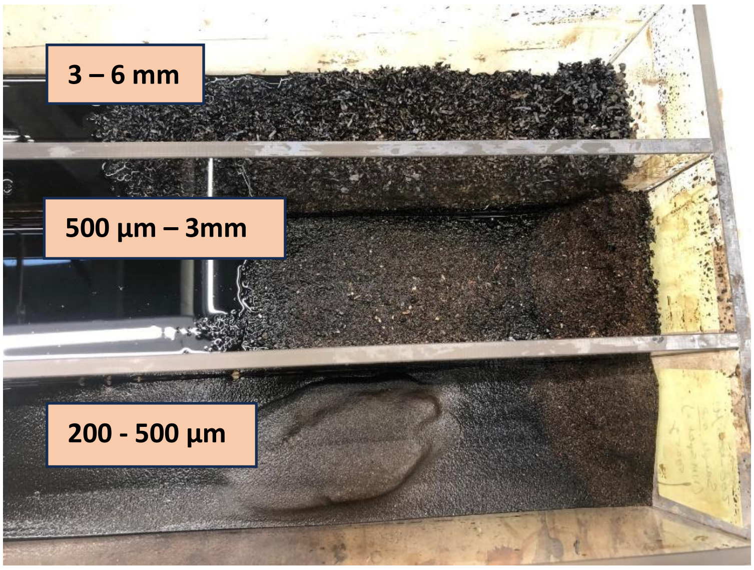

Figure 10: shows the product of material separation after MDS for the three particle sizes (200-500 µm), (500 µm -3mm) and (3 – 6 mm).

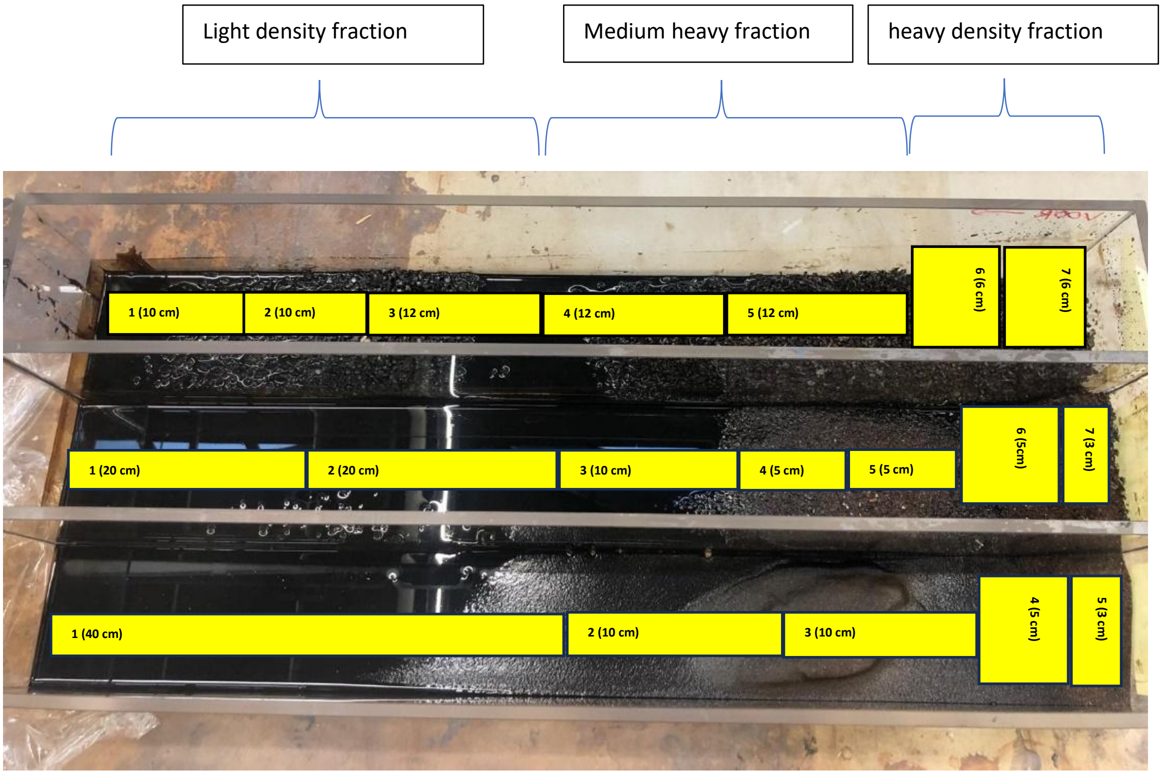

Figure 11: MDS container with the scrape off lengths for each sample analyzed for the three different particle sizes.

MDS product

Each feedstock size (Figure 10) was divided into subsamples (see Figure 11), with some subsamples weighing more than others, due to the varying suspension of particles at different positions within the container. The scraping process was conducted from the right side to the left side of the container to minimize the mixing of light-density and heavy-density particles. The scrape-off lengths varied, with shorter lengths on the left side and longer lengths on the right side. This approach was necessary because heavier metal particles, with higher densities, tended to accumulate on the right side of the container, closer to the magnet, while lighter particles remained further away. The choice of different scrape-off lengths allowed for a more accurate representation of the separation process by capturing the density gradient across the container. After scraping, the subsamples were weighed, washed, and dried at 105°C before being weighed again to account for any material loss during washing. Once the mass of each fraction was documented, the samples were prepared for further analysis. A detailed mass balance of the procedure is provided in Appendix 1.

4.3. XRF analysis

Sample preparation

To ensure the accuracy and reliability of the x-ray fluorescence analysis (XRF), samples underwent a milling process aimed at minimizing particle size effects. Larger particles can cause relative errors and issue with accuracy in XRF measurements (See figure 12) due to the variation in X-ray absorption and scattering caused by particles size differences (Beckhoff et al., 2006). The samples were first grinded using a disk mill (image 1) to make sure the particles achieve a uniform and fine particle size distribution to ensure optimal homogeneity. After milling, the samples were sieved with a sieve size of 100 µm using a sieve shaker with an amplitude of 1.5 mm for 60 seconds (image 2).

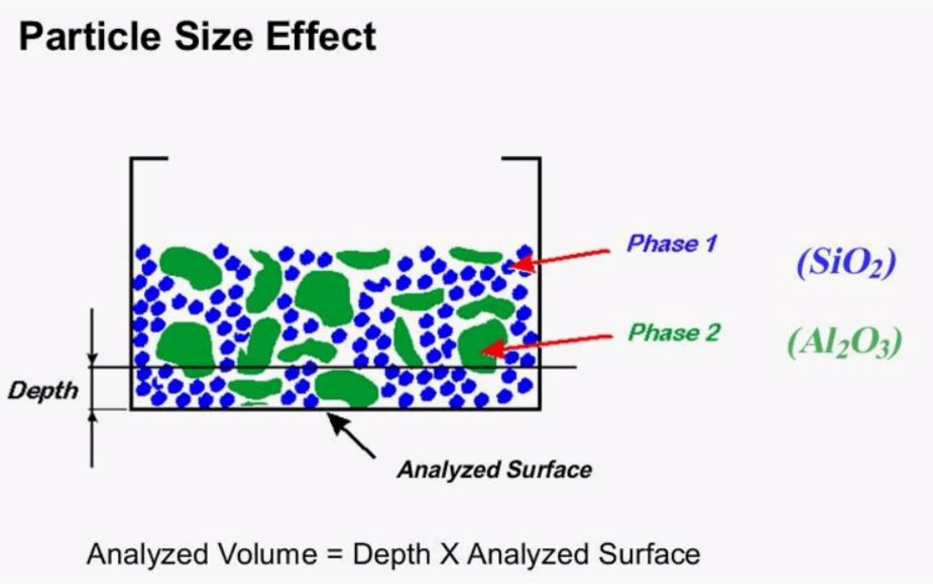

Figure 12: illustration of the particle size effect on the XRF analysis where the aluminum oxide particles (green) and the silicon dioxide particles are both measured in two phases but with two different analyzed surfaces due to particle size differences (Beckhoff, 2006).

After sieving, each sample was spilt into two fractions; the fraction that didn't pass through (>100 µm) and the fraction that did (<100 µm). For accuracy purposes it was decided to examine both fractions separate under the XRF. This would provide more clarity on the content recovery from each sample taken. Finally, the samples were pressed into pellets to further enhance homogeneity and ensure a flat, smooth surface for analysis.

All machines were used from the Stevin's laboratory at the faculty of Civil Engineering and Geosciences of the Delft University of Technology.

Image 1: disk mill to mill samples into powder.

Image 2: Sieve shaker for homogeneity.

Calibration

Before analyzing the sample, a calibration procedure was performed using six custom calibration standards. These standards were selected to closely match the matrix and composition of the analyzed samples. Each standard contained 5 to 6 trace metals of known concentrations, representative of the metals of interest in this study. By using high purity (see table 4) amounts of copper, zinc, tin, silicon, lead and silver. The calibration samples were divided into three heavy and three light standards. For each particle size two standards were prepared, one heavy and one light. the heavy standards would have larger amounts of copper, zinc, tin silver and lead. While the light standards would dominate in the amounts of silicon to the rest of the metals. The six samples were prepared with a very precise scale up to three decimal points and then milled to assure homogeneity before being examined by the XRF. The spectrometer response (intensity counts) was plotted against the known concentrations of the trace metals. A linear regression model was applied to generate the calibration curves, which were used to quantify the metal mass concentrations in the unknown samples (See figure 13).

Calibration standards	*Cu*	*Zn*	*Sn*	*Si02*	*Ag*	*Units*
Standard 1 (Ag 93% purity)	3.003	0.000	0.19	0.166	0.118	g
percentage	64.67	0.000	4.092	3.575	2.541	%
standard 2 (Ag 83% purity)	0.164	0.107	0.064	2.503	0.07	g
percentage	5.146	3.357	2.008	78.54	2.196	%
standard 3 (Ag 95% purity)	0.437	0.171	0.184	3.006	0.087	g
percentage	9.412	3.683	3.963	64.74	1.874	%
standard 4 (Ag 94% purity)	2.048	0.333	0.352	0.334	0.171	g
percentage	40.27	6.547	6.921	6.567	3.362	%
standard 5 (Ag 91% purity)	0.100	0.200	0.000	4.292	0.460	g
percentage (%)	1.980	3.959	0.000	84.96	9.105	%
standard 6 (Ag 92.1% purity)	4.574	0.000	0.246	0.260	0.150	g
percentage (%)	87.46	0.000	4.704	4.971	2.868	%

Table 4: show the composition of the calibration standards prepared for each of the five metals in gram and percentage.

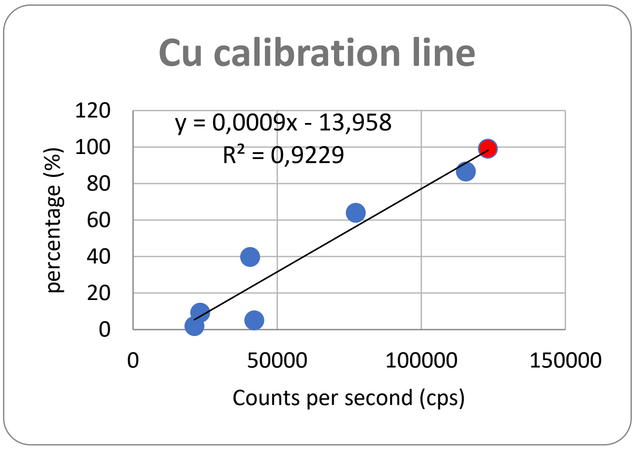

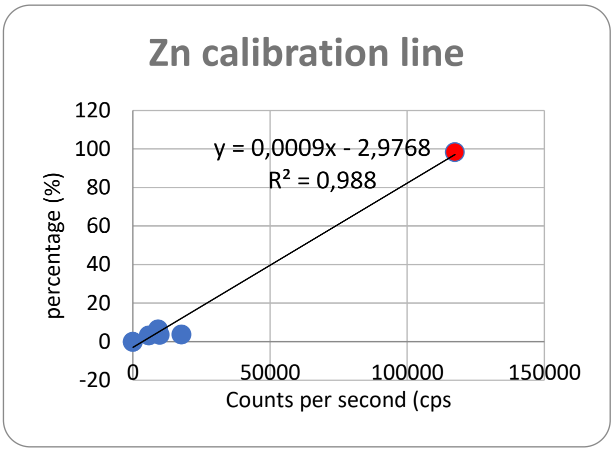

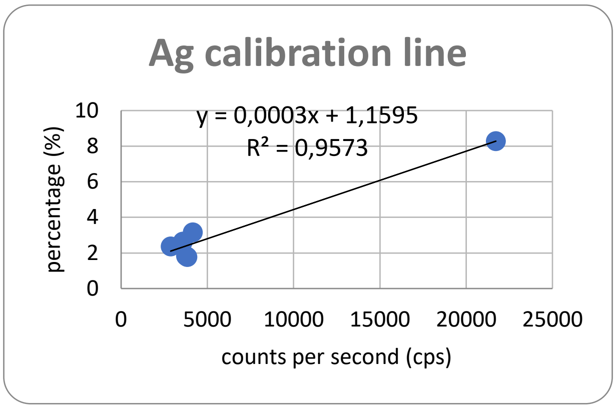

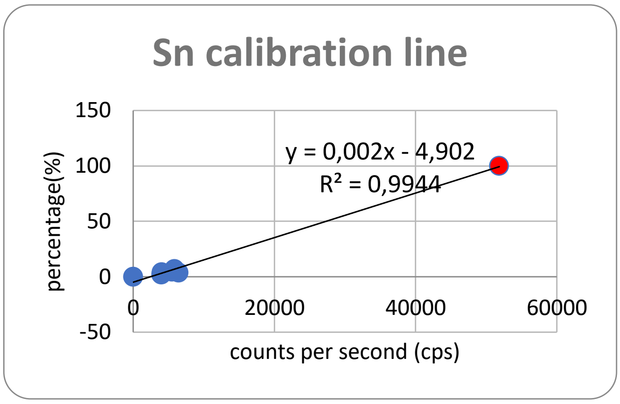

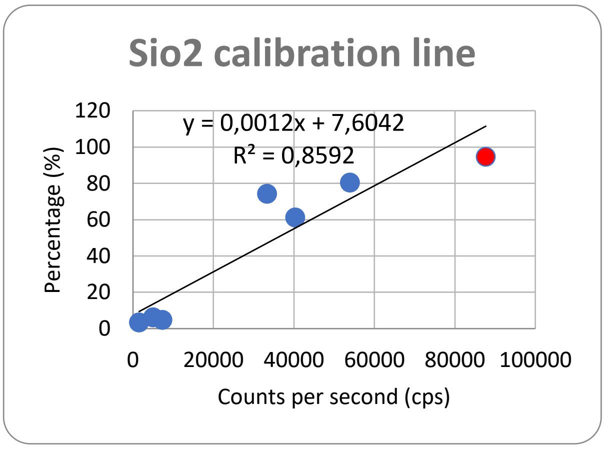

Figure 13: shows the five measured calibration curves for copper, zinc, tin, silver and silicon from right (up) to left (down). The red outliners are the individual measured concentrations of each target metal.

In addition to the custom prepared standards, the pure forms of each target metal were analyzed individually to establish the spectrometer's peak response for each metal. The intensity counts were incorporated into the calibration curves (see red outliners in figure 13) to ensure consistency and improved the reliability for trace metal detection. This was done for silicon, zinc, tin and copper (see table 5). Silver could not be analyzed alone as there was not a lot of silver metal available in pure form to be measured solely. The different purities for silver during calibration are mentioned next to the standards (table 5).

Metal	***Purity Percentage (%)***	***cps (counts per second)***
Silica (SiO_2)	94,512	87678,31
Zinc (Zn)	98,326	117426,4
Tin (Sn)	99,99	51851,56
Copper (Cu)	98,998	123191,1
Silver (Ag)		Not available

Table 5: high purity metals run through the XRF.

4.4. Data Analysis

Mass Balance of the separation process

The mass flow diagram (see appendix 1) represents the separation process for 100 kg of input material. Masses associated with wet sieving, drying, and magnetic separation are based on directly measured experimental values. However, the results from the Magnetic Density Separation (MDS) stage were scaled by a factor of approximately 16 (see table 6 below). This scaling was necessary because the MDS experiments were conducted on smaller sample masses (1/16) of the total amount (see figure 7), due to equipment and resource constraints. To ensure consistency with the larger upstream flows, the MDS results were multiplied by this scaling factor to match the total input of 100 kg.

	Experiment (in kg)	**Total input (in kg)**	**Scaling factor**
Sample 1	0,5905	9,819	16,628
Sample 2	1,111	17,819	16,039
Sample 3	0,9252	15,000	16,213

Table 6: shows the scaling factor used on the MDS results of the experiment.

According to the produced mass balance that is presented in appendix 1, the amount of metal recovered was calculated as:

$$\mathrm{M_{recovered}}\ (\%) = \left(\frac{\text{Mass of the metal in the separated fraction after the MDS}}{\text{Total mass before the MDS}}\right) x\ 100$$

Error calculations

For each metal recovery in the three samples, the following errors were taken into account:

Instrumental Error $E_{instrumental}$ (%): $\frac{\Delta M_{recovered}}{M_{recovered}}$ accounts for the measurement uncertainty in the XRF results ΔM_{input} was taken at 5%.

Measurement Error $E_{measurement}$ (%): $\frac{\Delta M_{input}}{M_{input}}$ reflects error in the input mass material loss ΔM_{input} = 5%. (e.g. weighing subsamples or sampling bias)

Material loss Error E_{loss} (%): $\frac{L}{100}$ where L is the material loss percentage during handling.

$$\Delta R = Recovery\ x\ \sqrt{E_{instrumental}^2 + +E_{measurement}^2 + E_{material\ loss}^2}$$

For the purity of the recovered metals the following errors have been taken into account:

Calibration Error $E_{calibration}$ (%): was measured as the standard error of regression which reflects potential inaccuracies in instrument calibration, quantifying the typical deviation of the measured standards.

$$E_{calibration} = \sqrt{\frac{\sum(y_i - \bar{y}_i)^2}{n-2}}$$

Uncertainty error $E_{uncertainity}$ (%): accounts for the reference standard uncertainty. Which is calculated as:

$$E_{uncertainity}(\%) = 100 - purity\ of\ metal\ standard$$

The $Separation\ efficiency$ was calculated based on the contamination, the amount of incorrect material present in each subsample to give an indication of the separation effectiveness of the MDS in separating light density from high density metals. The ideal scenario for the separation would be that the density of the metals, with lighter metals is expected to be separated further from the magnet and heavier materials closer to the magnet. Contamination is defined as the presence of materials that deviate from this expected density-based separation.

$$Separation\ Efficiency(\%) = \frac{Mass\ of\ targeted\ metal}{Total\ mass\ of\ fraction} x\ 100$$

Light-Density fraction:

The first and second subsamples (from the left) (see figure 14) are expected to primarily contain silicon (the lightest metal).

Contamination in these subsamples is defined as the presence of heavier metals (e.g., silver, copper, zinc, or tin).

Heavy-Density fraction:

The subsample closest to the magnet (last subsamples) should predominantly contain silver (the heaviest material) and further copper (see figure 14). Intermediate subsamples should primarily contain zinc and tin, based on their intermediate heavier densities.

Contamination in these subsamples is defined as the presence of silicon, copper and silver.

The effective separation for each metal was calculated for all three size range samples, considering the amount of light density materials (e.g., silicon) ending up in heavy-density subsamples and vice versa. The metals were separated horizontally in the MDS system, with the heaviest metal (silver) closest to the magnet and the lightest material (silicon) furthest from the magnet.

Assuming the errors are independent, the total error was calculated as:

$$\Delta SE = Seperation\ efficiency\ x\ \sqrt{E_{calibration}^2 + E_{uncertainity}^2}$$

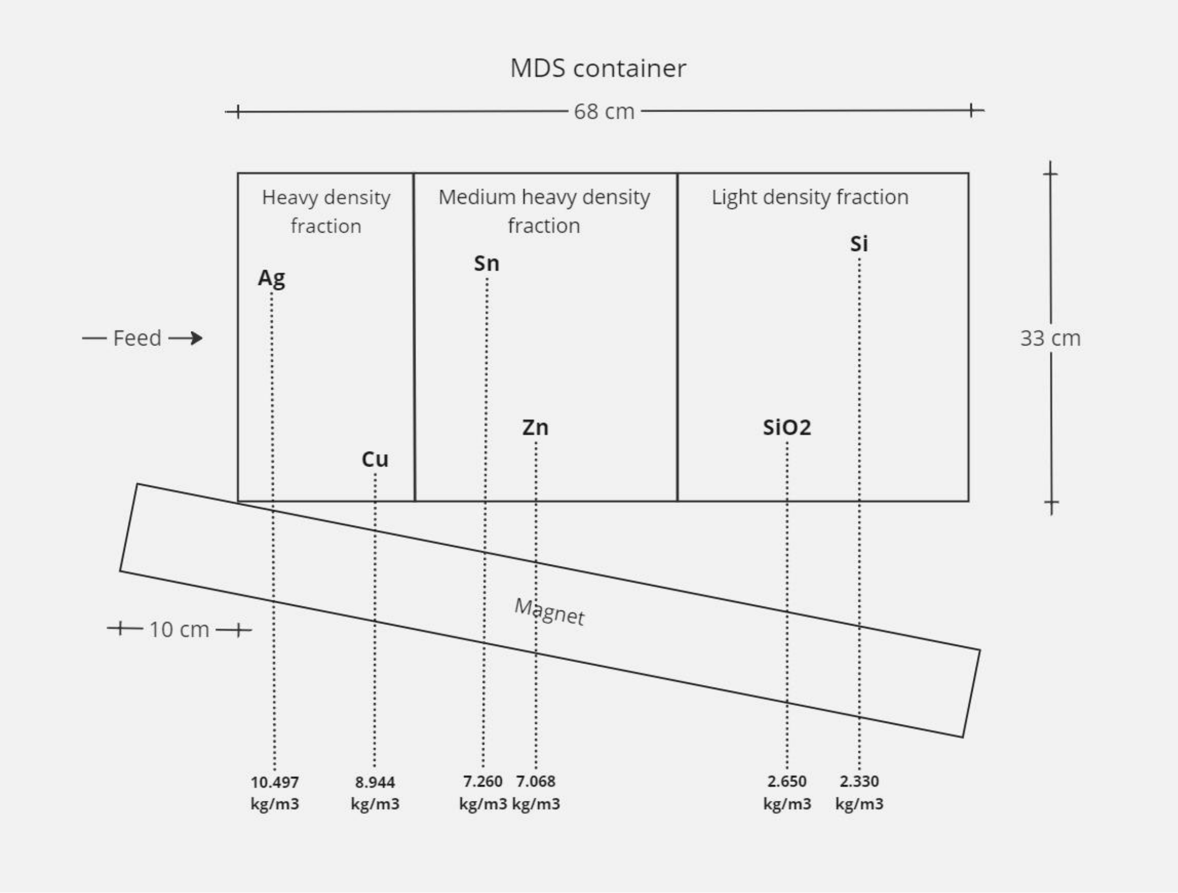

Figure 14: shows the illustration of the expected positions of sedimentation of the target metals according to their densities along the length of the container after MDS.

This was also done for the total recovery rate of all five metals for each sample to access the overall efficiency of the MDS separation. However, an additional error has been introduced due to upscaling which is important to take into consideration:

$$E_{combined\ recovery} = \sqrt{\sum_{i=1}^{n} E_{recovery}^2, i}$$

$E_{recovery}^2, i$: The recovery rate error for metal i.

n: The total number of metals in a sample

$$E_{total} = \sqrt{E_{combined\ recovery}^2}$$

Financial snapshot of the MDS process (pilot scale)

A pilot-scale MDS process was designed and sponsored by MYNE, formely Reukema, a metal recycling company at the recycling lab of TU delft. The prototype is expected to process 1.5 tonnes an hour. In this controlled environment, data on energy consumption, material recovery, and operational costs were collected through my own experiment results, interviews and local information from the internet to simulate full-scale economic feasibility of the separation process. The maximum cost per ton calculation is based on balancing total process costs with the potential market value of recovered materials.

Components of the snapshot

The analysis is structured to reflect the unique conditions of a pilot-scale operation. Key cost categories include:

Fixed Costs

Equipment costs: MDS system (Magnet, tank and conveyer belt), additional equipment costs.

Maintenance costs: small-scale equipment wear-and-tear, cleaning agents, possible replacement.

Depreciation was not taken into account for simplicity.

Variable Costs

Energy Costs: The lab-scale MDS system's energy consumption (measured in kilowatt-hours per ton processed) multiplied by the local electricity cost.

Labor Costs: Reflects time spent by lab personnel operating the system and conducting associated analyses, calculated using hourly wage rates.

Consumables: Includes total ferrofluid consumption and material input costs.

Material recovery revenue

The recovery efficiency for each metal (e.g., copper, zinc, tin, silver, silicon) is derived from experimental results for different particle size ranges. These efficiencies are combined with market prices (London metal exchange formulas) from the average of the last three years to calculate the total recovered value per ton of material processed.

The recovery value per sample is calculated as:

$$\sum Recovered\ mass\ per\ metal\ x\ Market\ price\ of\ metal\ x\ scaling\ factor$$

As a final step, a break-even analysis was conducted to determine the point at which the profitability of the pilot-scale Magnetic Density Separation (MDS) process exceeds the total costs. This analysis helps evaluate the economic feasibility of scaling the process to industrial levels.

The break-even point is calculated using the following relationship:

$$Break - Even\ Revenue = Total\ costs$$

Where:

$Total\ Costs$: Includes all input, operational, and capital costs per ton.

$Revenue$: Derived from the market value of recovered metals per ton of processed material.

Assumptions

- Market prices remain stable during the analysis period.
- The process operates under laboratory-scale efficiency levels.

Qualitative analysis of magnetic fraction

The magnetic fraction for the 0-3 mm samples was chosen to be analyzed to detect the presence of any of the targeted non-ferrous metals that could indicate incomplete separation. Their presence could reduce the recovery efficiency of the target non-ferrous metals in subsequent processing (MDS). This was to assess whether proper separation could improve the recovery of non-ferrous target metals in the finer particles size range. Smaller particle sizes tend to be challenging due to agglomeration with non-ferrous particles. The flow diagram of this process is presented in figure 15.

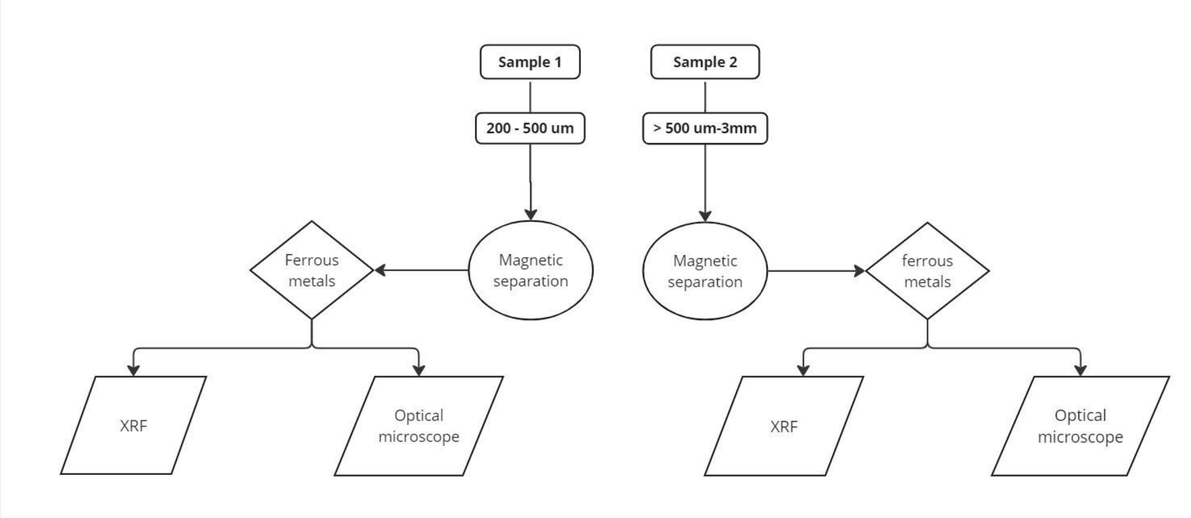

Figure 15: process diagram for the analysis of the magnetic fraction of particle sizes 0-3 mm.

To prepare the magnetic metal concentrate, two different leaching solutions were used to remove the corroded layer on the particles for comparison. The goal was to dissolve surface rust without completely dissolving the iron. A 0.1 mol/L HCl solution and a 0.26 mol/L citric acid solution were applied to particle size samples of 200–500 µm and >500 µm–3 mm (see image 5). The samples were submerged in both solutions for 30 minutes, dried, and analyzed without milling to evaluate the extent of non-ferrous metal adhesion to ferrous metals. Skipping the milling step allowed for a more accurate assessment of the separation process. The samples were then examined using an optical microscope (Keyence VHX-7000), capable of 6000x magnification and 4K high-resolution imaging, to validate the XRF analysis (see Image 4).

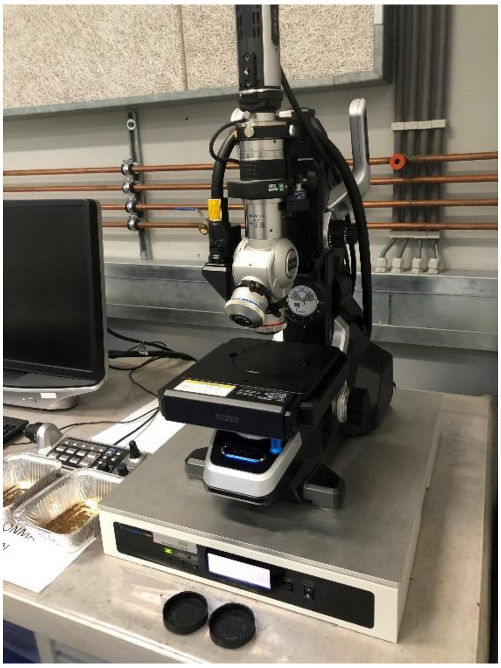

Image 4: microscope Keyence VHX-7000.

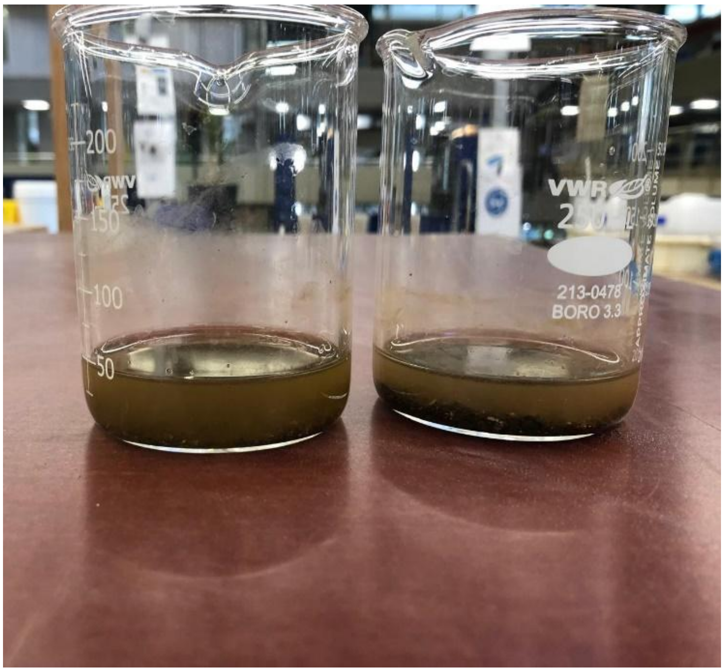

Image 5: shows submerged magnetic samples in diluted HCL (right) and citric acid (left).

5. Results and discussion

MDS products

The observed separation effectiveness and recovery rates for each metal in all three particle size ranges are summarized in tables 7, 8 and 9.

Sample 1 (200-500 µm)

Metal	***Density class***	***Separation efficiency %***	***Recovery rate, % (Experiment input)***	***Potential recovery, kg (100 kg input)***
Silica *(Si02)*	Light	88 ± 17	31.2 ± 7.2	2.31 ~ 3.75
Zinc *(Zn)*	Medium - heavy	0.7 ± 6.2	1.27 ± 0.29	0.122 ~ 0.128
Tin *(Sn)*	Medium - heavy	1 ± 78	1.81 ± 0.42	0.174 ~ 0.182
Copper *(Cu)*	Heavy	13 ± 12	24.5 ± 5.6	1.85 ~ 2.88
Silver *(Ag)*	Heavy	1.4 ± 8.8	1.09 ± 0.25	0.099 ~ 0.104
Total			59.9 ± 9.1	2.96 ~ 4.09

Tabel 7: shows the results of the total recovery of each metal in sample 1 and the corresponding purity of each fraction according to density class.

In sample 1 (figure 16), silica (SiO_2) in the form of sand was predominantly found in the lighter fractions (subsamples 1.1, 1.2 and 1.3) (image 6), with a high separation effectiveness of 88 ± 17% and a high recovery rate of 31.2 ± 7.2% considering it to be one of the dominating metals in the sample. Unexpectedly, silica was also present in smaller amounts in heavier fractions, including subsamples 1.4 and 1.5. The potential recovery of silica assuming a waste input of 100 kg varied between 2.31 and 3.75 kg.

Zinc (Zn), expected to dominate in the medium-heavy fractions subsamples 1.3 and 1.4 (image 6), primarily observed in subsample 1.3 was also found in considered amounts in subsample 1.5. The separation effectiveness was 0.7 ± 6.2%, and the recovery rate was 1.27 ± 0.29%. Its distribution

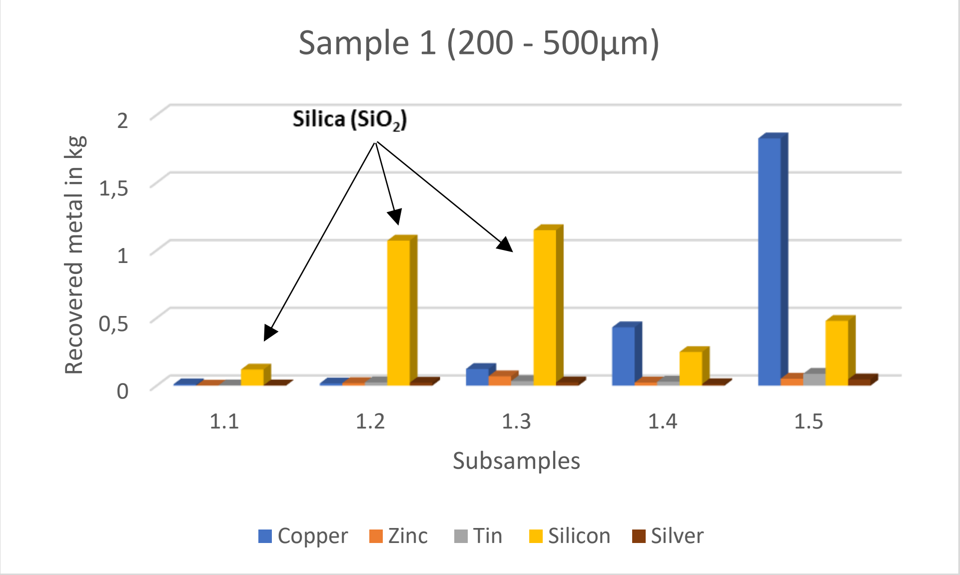

Figure 16: shows the separation of five target metals with MDS for sample 1. From left (furthest from the magnet) to the right (closest to the magnet).

indicates partial alignment with density expectations. This was also the observation for Tin (Sn) which was also anticipated in the medium-heavy fractions, showing significant deviations in its occurrence in different other subsamples and being largely found in subsample 1.5, alongside silver and copper, the heaviest density range. The separation effectiveness and the recovery rate are at 1 ± 78% and 1.81 ± 0.42% respectively. The potential recovery for zinc varies between 0.122 and 0.128 kg and for tin between 0.174 and 0.182 kg.

Copper (Cu), a separation effectiveness of 13 ± 12%, was mostly distributed across subsamples 1.3, 1.4, and 1.5, with significant amounts in each resulting in poor separation overall. The recovery rate of copper is at 24.5 ± 5.6%, the second highest after silicon among all metals in Sample 1. Its potential recovery varies between 1.85 and 2.88 kg.

Silver (Ag) existing already in very small amounts, achieved a decent recovery of 1.09 ± 0.25%. The metal was concentrated primarily in subsample 1.5 but not exclusively. Unfortunately, substantial amounts were also found in lighter density subsamples (1.2 and 1.3). Its separation effectiveness is observed at 1.4 ± 8.8% and its potential recovery varies between 0.099 and 0.104 kg.

The total recovery rate of all five metals is at 59.9 ± 9.1 resulting in a potential recovery between 2.96 and 4.09 kg of the total amount of metals recovered from sample 1.

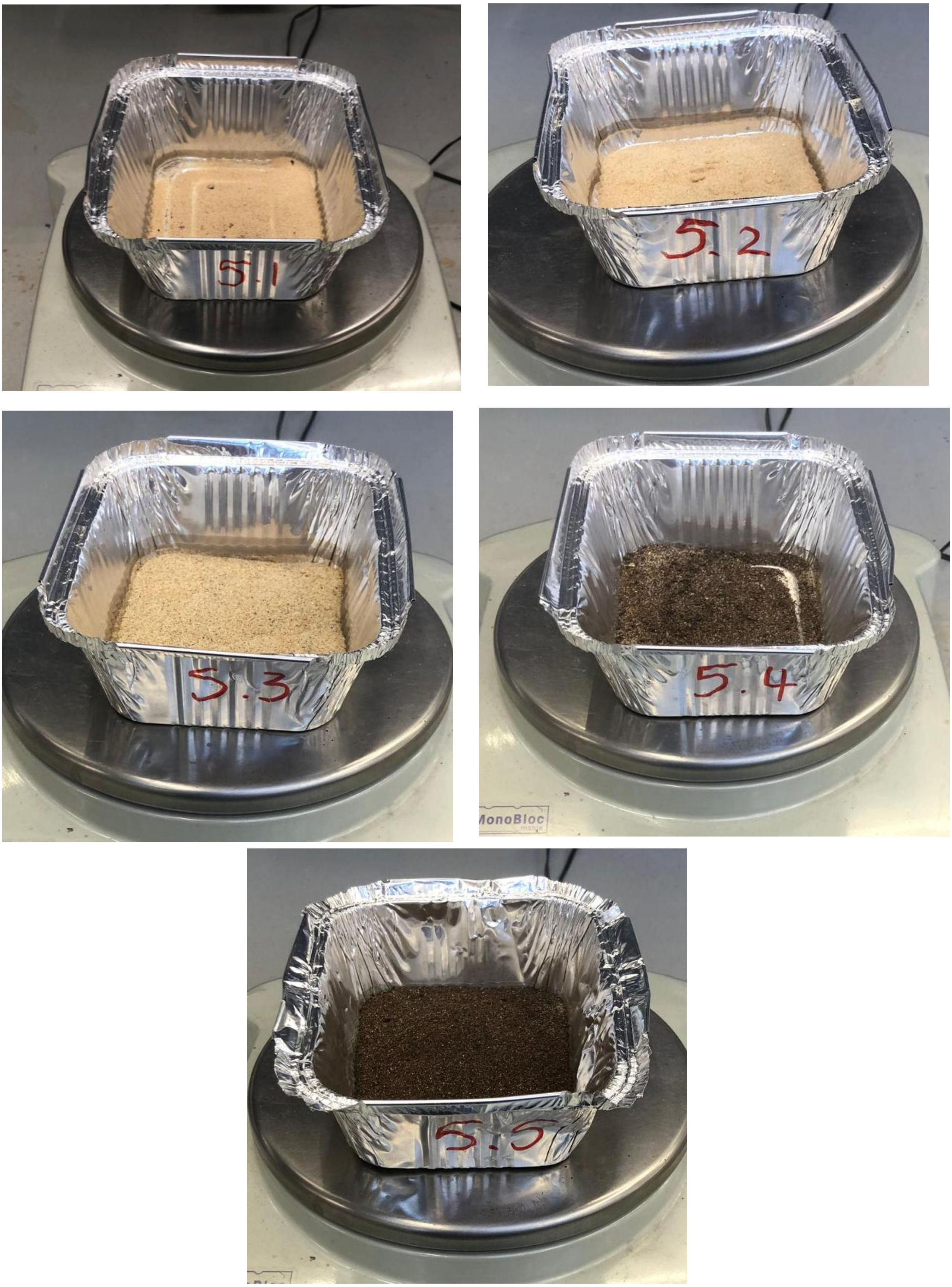

Image 6: shows the recovered subsamples from sample 1 (1.1 (as 5.1),1.2 (as 5.2), 1.3 (as 5.3) consisting mostly of sand particles (yellow color), in sample 1.3 (as 5.3) you can see some dark-colored particles mixed in the sand. In subsample 1.4 (as 5.4) shows mostly copper particles mixed with small amounts of sand and in 1.5 (5.5) the subsample shows a mostly black-reddish color from the copper particles.

Sample 2 (>500 µm – 3mm)

Metal	***Density class***	***Separation efficiency %***	***Recovery rate, % (Experiment input)***	***Potential recovery, kg (100 kg input)***
Silica *(SiO2)*	Light	47 ± 17	3.57 ± 0.17	0.634 ~ 0.638
Silicon *(Si)*	Light	31.1 ± 5.5	15.5 ± 0.76	2.75 ~ 2.77
Zinc *(Zn)*	Medium-heavy	31.1 ± 6.2	3.1 ± 0.15	0.551 ~ 0.554
Tin *(Sn)*	Medium - heavy	33 ± 78	1.28 ± 0.06	0.228 ~ 0.229
Copper *(Cu)*	Heavy	1 ± 12	69.3 ± 3.4	11.8 ~ 12.5
Silver *(Ag)*	Heavy	0.8 ± 8.8	1.19 ± 0.06	0.212 ~ 0.213
Total			93.9 ± 3.5	14.3 ~ 15.5

Tabel 8: shows the results of the total recovery of each metal in sample 1 and the corresponding purity of each fraction according to density class.

In sample 2 (figure 17), silicon dioxide (SiO_2) was found in the first subsamples (2.1 and 2.2) which was mostly in the form of glass (see image 7). The separation effectiveness of SiO_2 is observed at a fair 47 ± 17%, with a recovery rate of 3.57 ± 0.17% indicating good separation of glass (light density) from the rest of the metals (heavier densities). On the other hand, the silicon (Si) was distributed over all the subsamples showing the highest amount in subsample 2.7. The separation effectiveness is a 31.1 ± 5.5% with a recovery rate of 15.5 ± 0.76% confirming poor separation from the lighter density fraction (subsamples 2.1 and 2.2) but higher in quality as the error in recovery was smaller than in sample 1 resulting in higher recoveries in mass varying potentially between 0.634 and 0.638 kg.

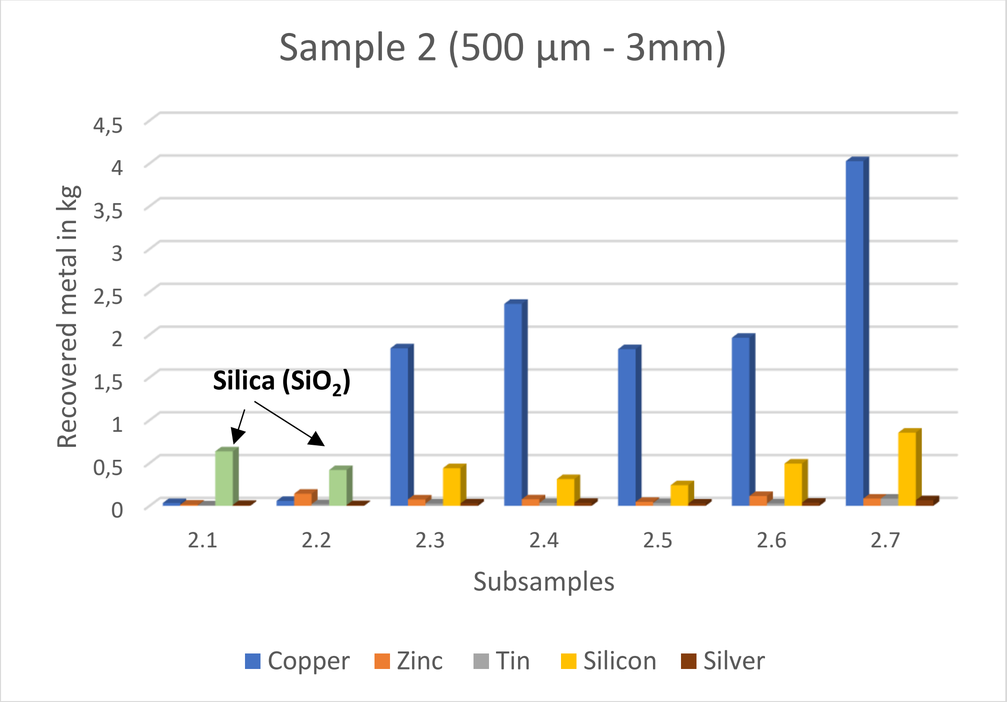

Figure 17: shows the separation of five target metals with MDS for sample 2. From left (furthest from the magnet) to the right (closest to the magnet).

Zinc (Zn) was unexpectedly most abundant in subsample 2.2, a lighter density fraction, which is a deviation from the expected for a medium-heavy density metal. Its second-highest amount was found in subsample 2.6, while the rest was distributed across the rest of the lighter subsamples in smaller amounts. The separation effectiveness for zinc is fairly at 31.1 ± 6.2%, with a recovery rate of

3.1 ± 0.15%. The potential recovery varied between 0.551 and 0.554 kg the highest recovery of zinc from the three samples analyzed.

Tin (Sn), expected to concentrate in the medium-heavy fractions was found again in low quantities across subsamples and again primarily alongside silver in subsample 2.7. Tin's separation effectiveness of 33 ± 78% is much higher than in sample 1, and its recovery rate is at 1.28 ± 0.06% slightly lower than in sample 1. The potential recovery calculations varied between 0.228 and 0.229 kg higher than in sample 1.

Copper (Cu) achieved the highest recovery rate among all metals at 69.3 ± 3.4%, with a poor separation effectiveness of 1 ± 12%. due to its presence across multiple medium heavy density subsamples (2.3, 2.4, 2.5). Copper was predominantly located in subsample 2.7 as well, the heaviest metal density subsample alongside Silver (Ag) which was also concentrated mainly in 2.7 consistent with its heavy density. However, poor separation was evident as silver was also found in the rest of the (lighter) subsamples. The separation effectiveness is much lower than in sample 1 at 0.84 ± 8.82% but showing a much higher recovery rate of 1.19 ± 0.06% considering a lower error. The potential recovery of copper varied between 11.8 and 12.5 kg and for silver between 0.212 and 0.213 kg.

The overall recovery rate is much higher than sample 1 and is observed at a high 93.9 ± 3.5 resulting in a potential recovery between 14.3 and 15.5 kg of metals in sample 2.

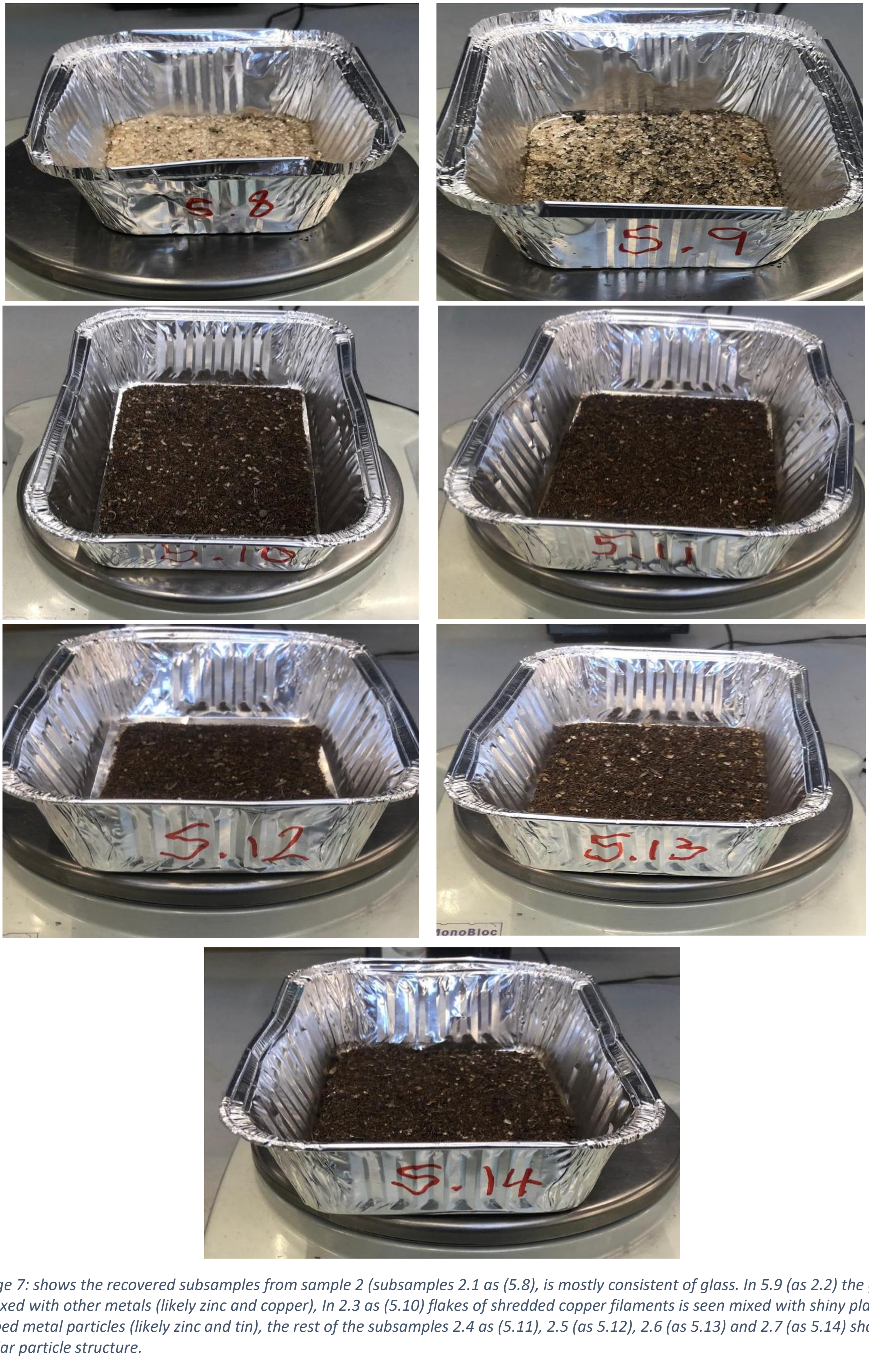

Image 7: shows the recovered subsamples from sample 2 (subsamples 2.1 as (5.8), is mostly consistent of glass. In 5.9 (as 2.2) the glass is mixed with other metals (likely zinc and copper), In 2.3 as (5.10) flakes of shredded copper filaments is seen mixed with shiny plate shaped metal particles (likely zinc and tin), the rest of the subsamples 2.4 as (5.11), 2.5 (as 5.12), 2.6 (as 5.13) and 2.7 (as 5.14) shows a similar particle structure.

Sample 3 (>3mm - 6mm)

The MDS process for Sample 3 exhibited notable trends and deviations in metal distributions across subsamples. The separation effectiveness and recovery rates for each metal are as follows:

Metal	***Density class***	***Separation efficiency %***	***Recovery rate, % (Experiment input)***	***Potential recovery, kg (100 kg input)***
Silica *(Si02) (glass)*	Light	93 ± 17	20.9 ± 0.76	3.138 ~ 3.146
Silicon *(Si)*	Light	0.0 ± 5.5	10.7 ± 0.39	1.596 ~ 1.604
Zinc *(Zn)*	Medium heavy	0.9 ± 6.2	1.31 ± 0.048	0.191 ~ 0.201
Tin *(Sn)*	Medium heavy	4 ± 78	8.34 ± 0.3	1.249 ~ 1.255
Copper *(Cu)*	Heavy	37 ± 12	59.9 ± 2.2	8.978 ~ 9.022
Silver *(Ag)*	Heavy	0.8 ± 8.8	1.63 ± 0.059	0.239 ~ 0.251
Total			81.9 ± 2.4	9.8 ~ 10.4

Tabel 9: shows the results of the total recovery of each metal in sample 3 and the corresponding purity of each fraction according to density class.

In sample 3 (figure 18), Silica (SiO_2) in the form of glass was primarily located in subsamples 3.1, 3.2, and 3.3 (see image 8), consistent with its light density range. Its separation effectiveness is at 93 ± 17%, with a recovery rate of 20.9 ± 0.76%, reflecting an efficient separation with a potential between 3.138 and 3.146 kg.

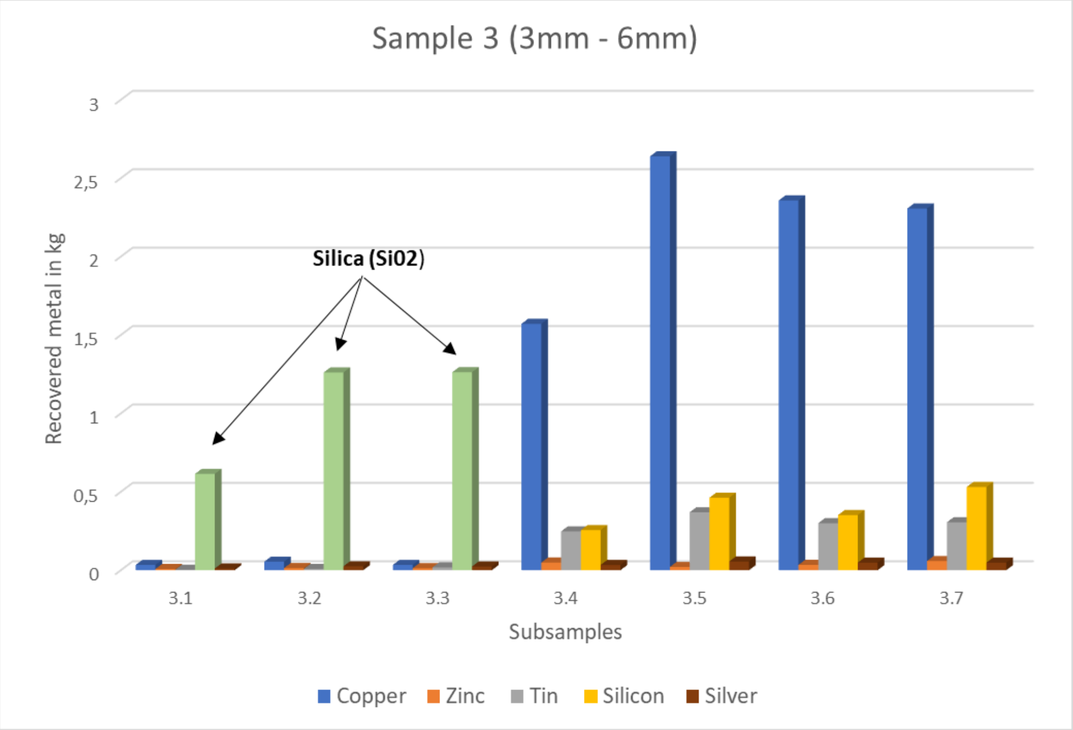

Figure 18: shows the separation of five target metals with MDS for sample 3. From left (furthest from the magnet) to the right (closest to the magnet).

Silicon (Si), however, was again unexpectedly distributed across the heavier subsamples rather than being concentrated in the lighter fractions. From its separation effectiveness of 0.00 ± 5.50% it is considered not separated, with a recovery rate of 10.7 ± 0.388% and a potential recovery varying between 1.596 and 1.604 kg.

Zinc (Zn) was predominantly found in subsample 3.7, with significant amounts also observed in subsample 3.4. This distribution indicates partially efficient separation, as zinc should ideally dominate the medium-heavy fractions. Its separation effectiveness is 0.855 ± 6.24%, and the recovery rate is at 1.31 ± 0.048% resulting in potential recovery amount between 0.191 and 0.201 kg.

Tin (Sn) was recovered in larger amounts compared to Samples 1 and 2. It was predominantly located in subsample 3.5 as expected, but also appeared in substantial quantities in subsamples 3.4, 3.6, and 3.7. The separation effectiveness for tin is a 4.34 ± 77.9%, with the highest recovery rate of 8.34 ± 0.303% compared to sample 1 and 2. Tin's potential recovery varied between 1.249 and 1.255 kg.

Copper (Cu) was again distributed across the higher density subsamples (3.4, 3.5, 3.6, and 3.7), with the majority found in subsample 3.6. Also, achieved the highest recovery rate among all metals in Sample 3, at 59.9 ± 2.17% with a potential recovery amount between 8.978 and 9.022 kg, but not higher than in sample 2. However, the separation effectiveness was in this sample higher than in sample 1 and 2 at 37.2 ± 12.3%.

Silver (Ag), primarily concentrated in subsample 3.5, showed poor and incomplete separation once again, as smaller amounts were observed in almost all subsamples. Its separation effectiveness is at 0.76 ± 8.82%, but has the highest recovery rate of 1.63 ± 0.059% compared to samples 1 and 2. A potential mass recovery calculated between 0.239 and 0.251 kg.

The overall recovery rate for sample 3 is at 81.9 ± 2.35 much lower than sample 2 and higher than sample 1 with the lowest error. The potential recovery of all metals is between 9.8 and 10.4 kg in sample 3.

The overlapping presence of all metals across subsamples reflects challenges in achieving ideal separation in all three particle size ranges. These results highlight the influence of factors such as particle interaction, alloy presence, or process limitations, which will be explored further in the discussion.

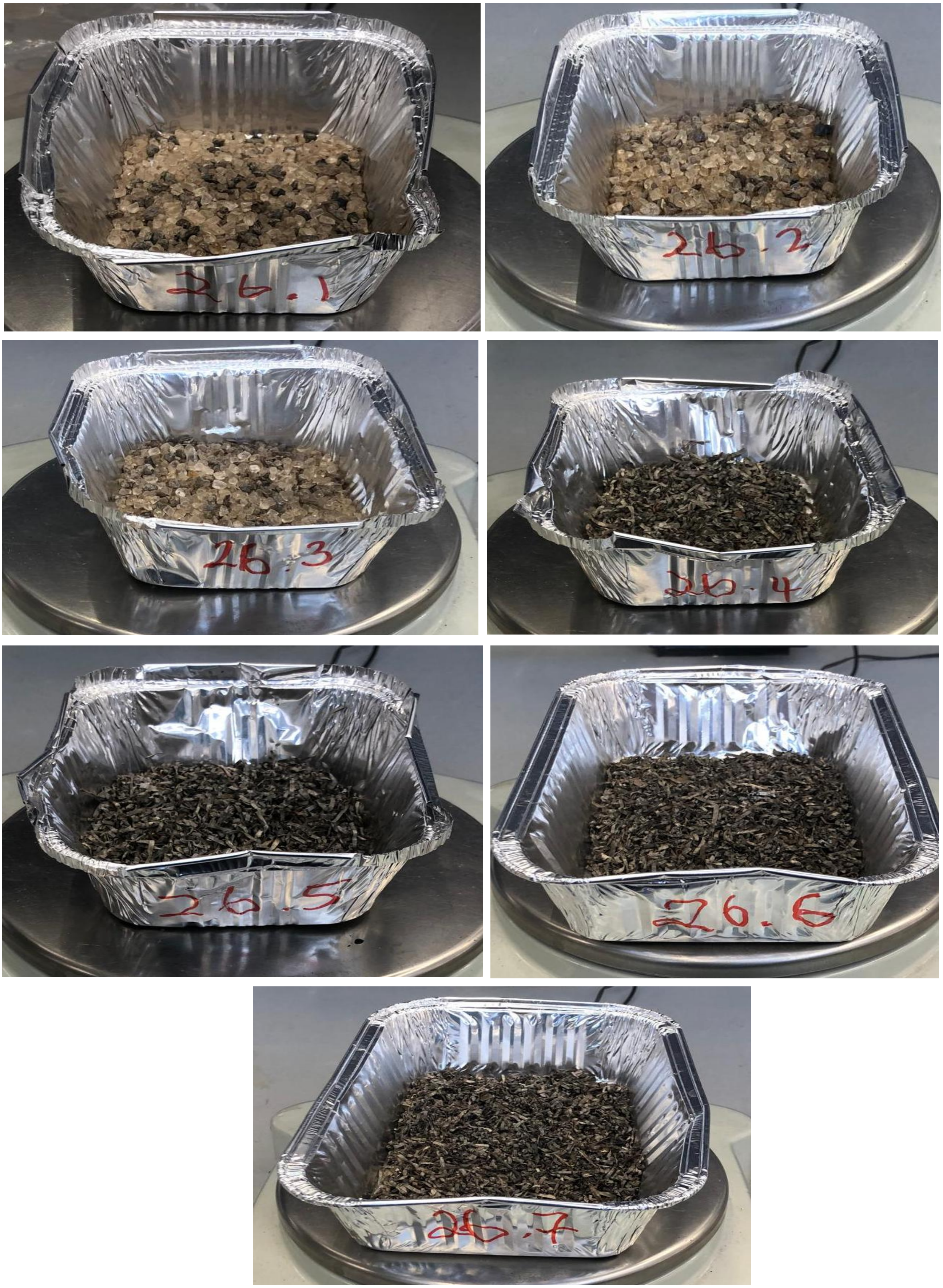

Image 8: shows the recovered subsamples from sample 3 (3.1 as 26.1, 3.2 as 26.2, 3.3 as 26.3) show a consistency of glass mixed with dark grained particles. The rest of the subsamples (3.4 as 26.4, 3.5 as 26. 5, 3.6 as 26.6, 3.7 as 26.7) show a mix of metal filaments of a grey brownish color (likely copper mixed with tin).

Financial snapshot: MDS process (pilot scale)

This section presents a very simple analysis focusing on key metrics like revenue, costs and profitability for the Magnetic Density Separation (MDS) process, scaled up to a throughput of 1 tonne of PV waste per hour processed over a year. Assuming optimal separation efficiency (≥95%), the recovered values of each metal per ton of PV waste have been calculated based on the adjusted recovery values for (100 kg throughput) in tables 10 and 11. The scaled-up (factor 10) recovery rates are shown in the table below: (for simplicity the errors were neglected).

Metal	Sample 1 (in kg)	Sample 2 (in kg)	Sample 3 (in kg)
Copper	24.119	121.229	90.048
Zinc	1.072	5.522	2.958
Tin	1.777	2.369	11.194
Silicon	31.278	29.734	17.390
Silver	1.127	2.337	2.843
Others (loss)	38.817	17.000	25.567
Total recovery	**98.190**	**178.190**	**150.000**

Table 10: summarizes the recovery of each metal in samples 1,2 and 3 assuming a throughput of 1 tonne/hr.

These values were then multiplied by current scrap market prices (see appendix 2) to estimate the revenue generated per ton of processed material.

The following table summarizes the financial performance for each metal per sample:

Metal	Sample 1	Sample 2	Sample 3
Copper	€ 172,63	€ 867,69	€ 644,52
Zinc	€ 1,83	€ 9,43	€ 5,05
Tin	€ 25,34	€ 33,79	€ 159,65
Silicon	€ 523,97	€ 498,10	€ 291,31
Silver	€ 766,40	€ 1.588,98	€ 1.933,24
Total revenue	**€ 1.490,17**	**€ 2.997,98**	**€ 3.033,77**

Table 11: summarizes the revenue of each metal in samples 1, 2 and 3 assuming a throughput of 1 tonne/hr.

The cost breakdown of the total costs for an MDS process for a throughput of 2000 tonnes/year are shown in table 12 below:

Fixed costs	MDS system	€ 300,000
	Additional equipment costs	€ 175,000
	Additional costs (25%)	€ 118,750
	Shovel or forklift	€ 87,500
	Maintenance cost	€ 1,250
Total fixed costs		€ 682.500
Variable costs	Building rent (500 m² hall)	€ 50,000
	Total Ferro-fluid costs	€ 3,900,000
	Total material costs	€ 240,000
	Labour	€ 120,000
	Energy and water costs	€ 13,860
Total variable costs		€ 3.023.860
Total costs		€ 3.706,360.00

Table 12: summarizes the fixed costs and variable costs for an MDS throughput of 1 ton per hour during 1 year (see appendix 2).

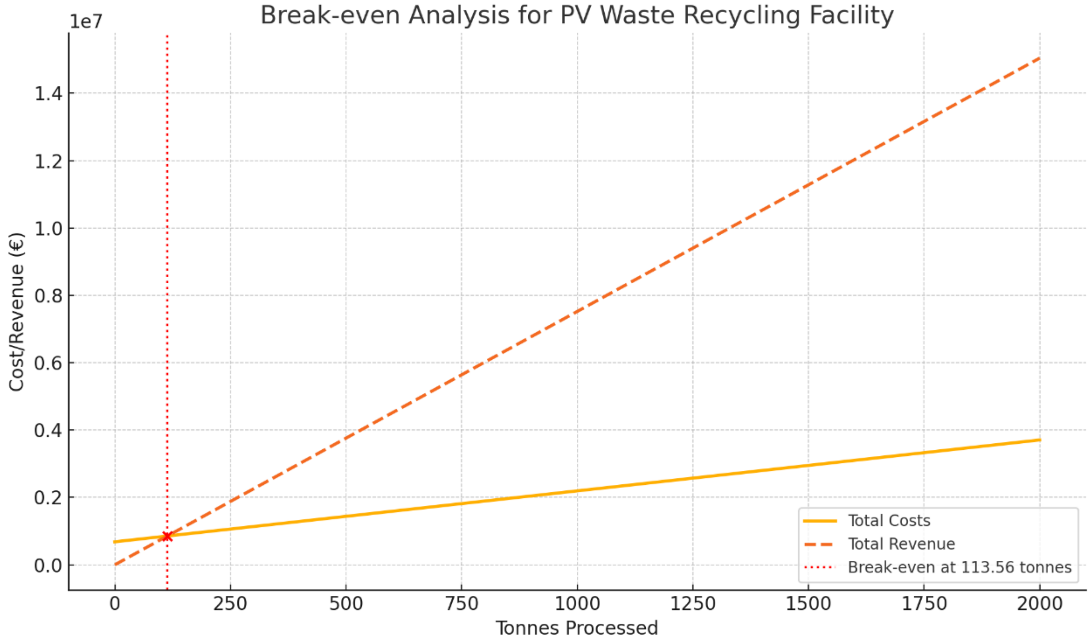

Figure 19: illustrates the Break-even analysis for a PV waste recycling facility with MDS processing 1 tonne per hour over 2000 hours per year.

The break-even analysis (figure 19) for the PV waste recycling facility illustrates the relationship between total costs and total revenue as a function of the tonnes of waste processed annually. The total costs curve includes both fixed and variable costs, while the total revenue curve reflects the revenue generated per tonne of processed material. The break-even point occurs at approximately 114 tonnes per year, indicating the facility needs to process just over 5% of its 2000 tonnes/year capacity to cover all costs. Beyond this point, every additional tonne processed contributes to profit, with a margin of approximately €6,010 per tonne. This early break-even threshold highlights the facility's strong profitability potential once the minimum processing volume is reached. The revenue calculated is excluding the profits from selling the dismantled aluminum alloy scrap from the from the panel frame.

The financial results of the Magnetic Density Separation (MDS) process reveal several key observations. Revenue is primarily driven by the recovery of silver and silicon, with silver contributing the highest revenue, particularly in Sample 3 (€1,933.24). Silicon also provides significant revenue across all samples, with its highest contribution in Sample 1 (€523.97). Copper, despite being recovered in large quantities, generates relatively less revenue due to its lower market value. Zinc and tin are recovered in smaller amounts and have minimal impact on overall revenue. The cost analysis highlights that variable costs specifically the costs for ferrofluid dominate the expense structure, totaling € 3,900,000/year taking into account that 90% of the ferrofluid can be recovered for a throughput of a ton of PV waste per hour.

Magnetic fraction (0 -3 mm)

Ferrous sample (200 – 500 µm)

The results of the ferrous separated fraction after samples were leached and analyzed with the XRF are shown in figure 20 and 21.

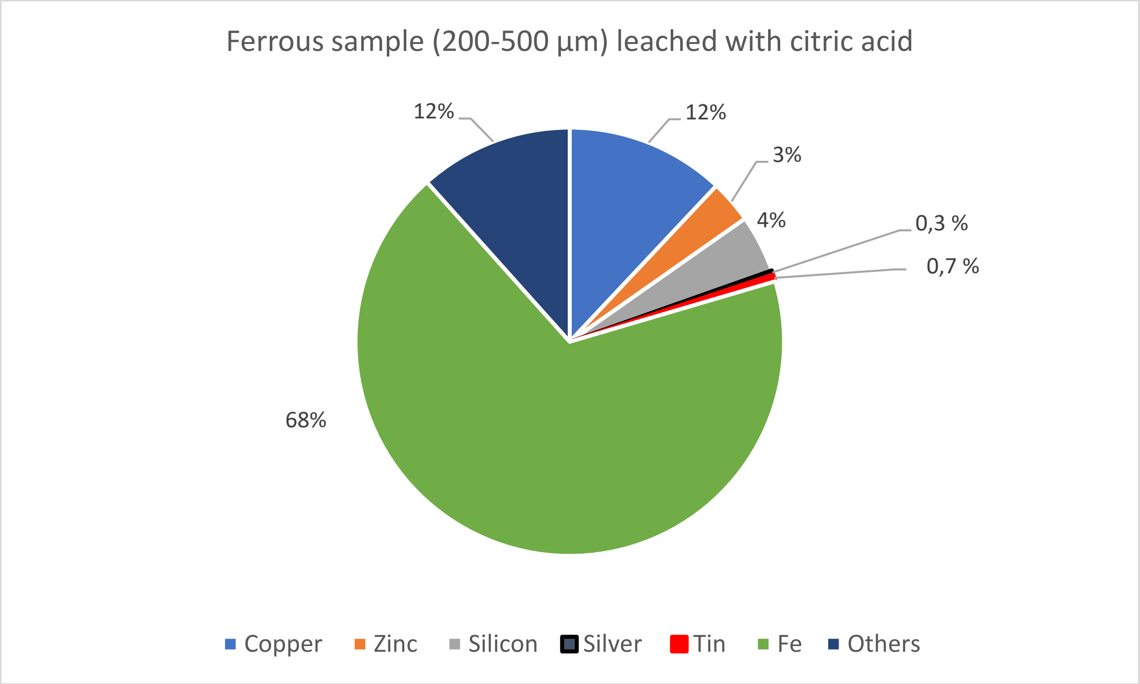

Figure 20: shows the results of the XRF analysis in mass concentration percentage for the sample leached with citric acid.

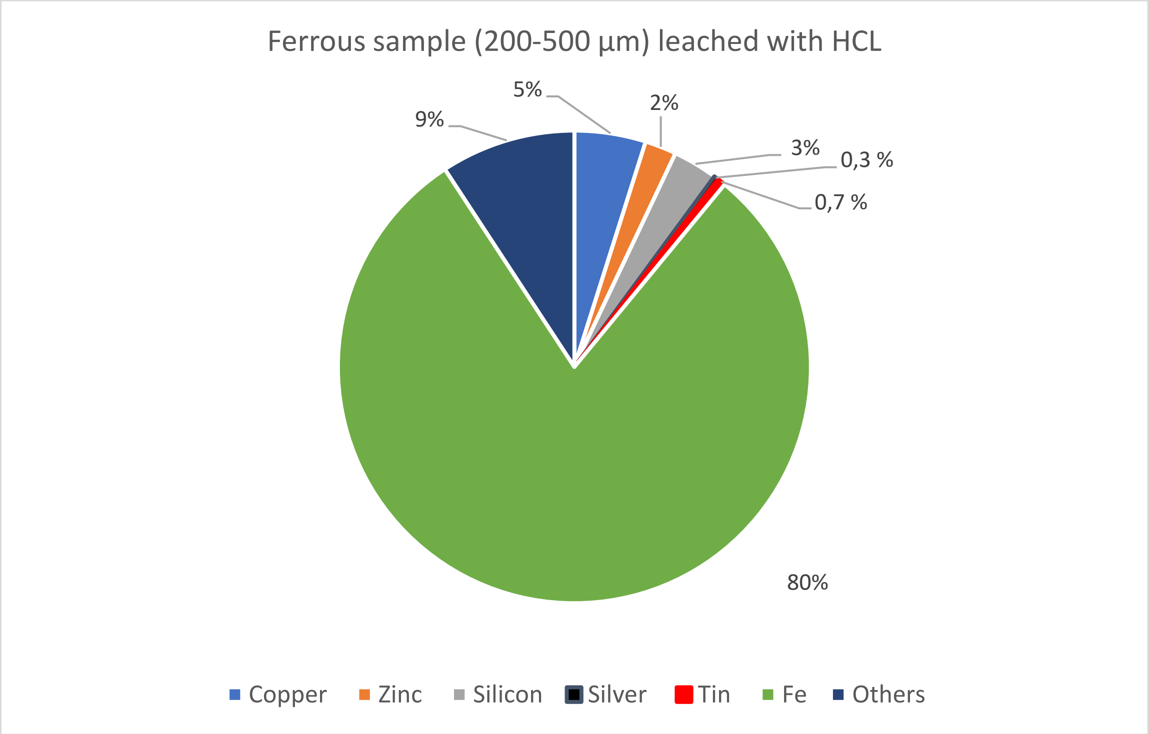

Figure 21: shows the results of the XRF analysis in mass concentration percentage for the sample leached with HCL.

Image 9: shows the pictures made by the optical microscope Keyence VHX-7000. (The upper picture the results after leaching with citric acid and the lower picture after HCL.). In the upper picture the particles appear to be a mix of oxidized materials, with a relatively rough texture and a predominately reddish-brown residue, likely indicating the presence of rust. Some particles exhibit a shiny, reflective surface, possibly metallic inclusions. The bottom image has a similar composition to the upper one, but the particles appear cleaner (less rust). More visible metallic inclusions can be seen scattered throughout the bottom sample.

The XRF data revealed that both samples leached are dominated by a high iron (Fe) content. However, contamination from non-ferrous metals varied, with HCl leaching showing lower levels of copper (5% vs. 12%), zinc (2% vs. 3%) and silicon (3% vs 4%) compared to citric acid. High-resolution images (image 9) confirmed that HCl was more effective at rust removal, exposing cleaner and more metallic surfaces, while citric acid-treated samples retained visible reddish-brown residues, likely indicating incomplete rust removal and potential retention of non-ferrous contaminants. The cleaner appearance of the HCl-leached particles is more likely to align with the lower contamination levels of non-ferrous metals observed in the XRF results. However, the lack of pre-leaching analysis is a potential limitation as the initial variability in the sample was not analyzed.

Ferrous sample (500 µm – 3mm)

The results of the ferrous separated fraction after samples were leached and analysed with the XRF are shown in figure 22 and 23.

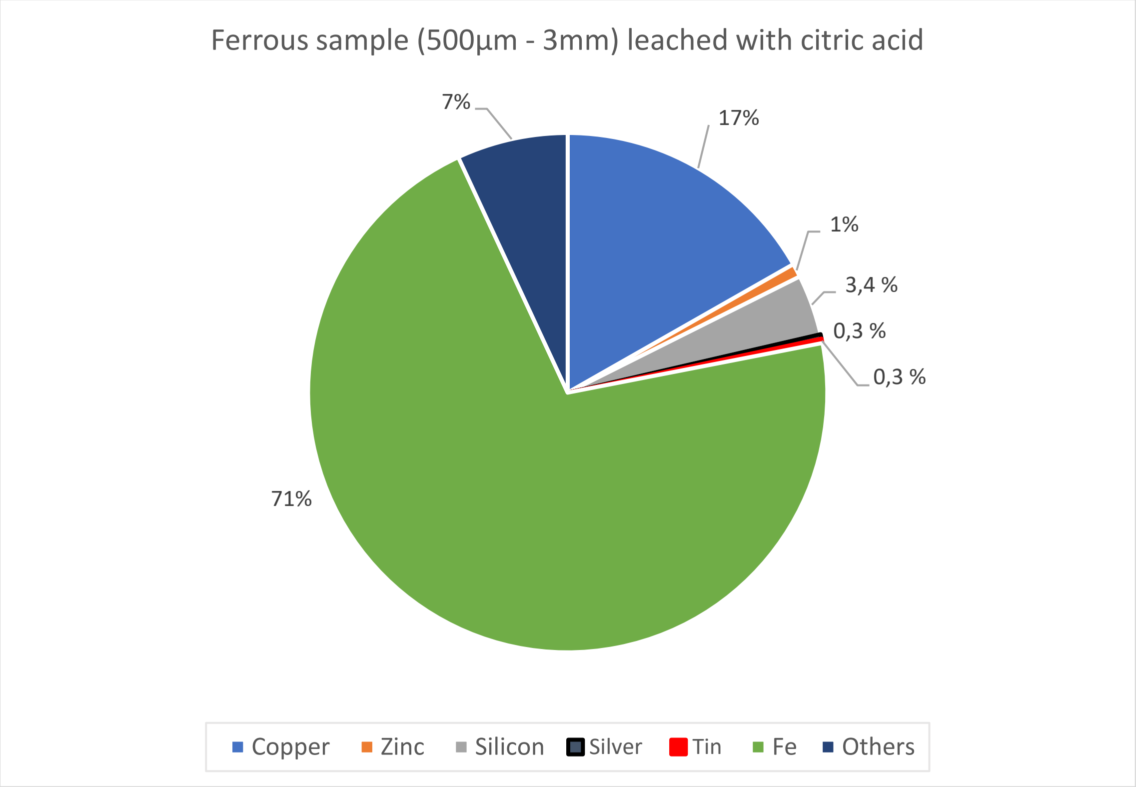

Figure 22: shows the results of the XRF analysis in mass concentration percentage for the sample leached with citric acid.

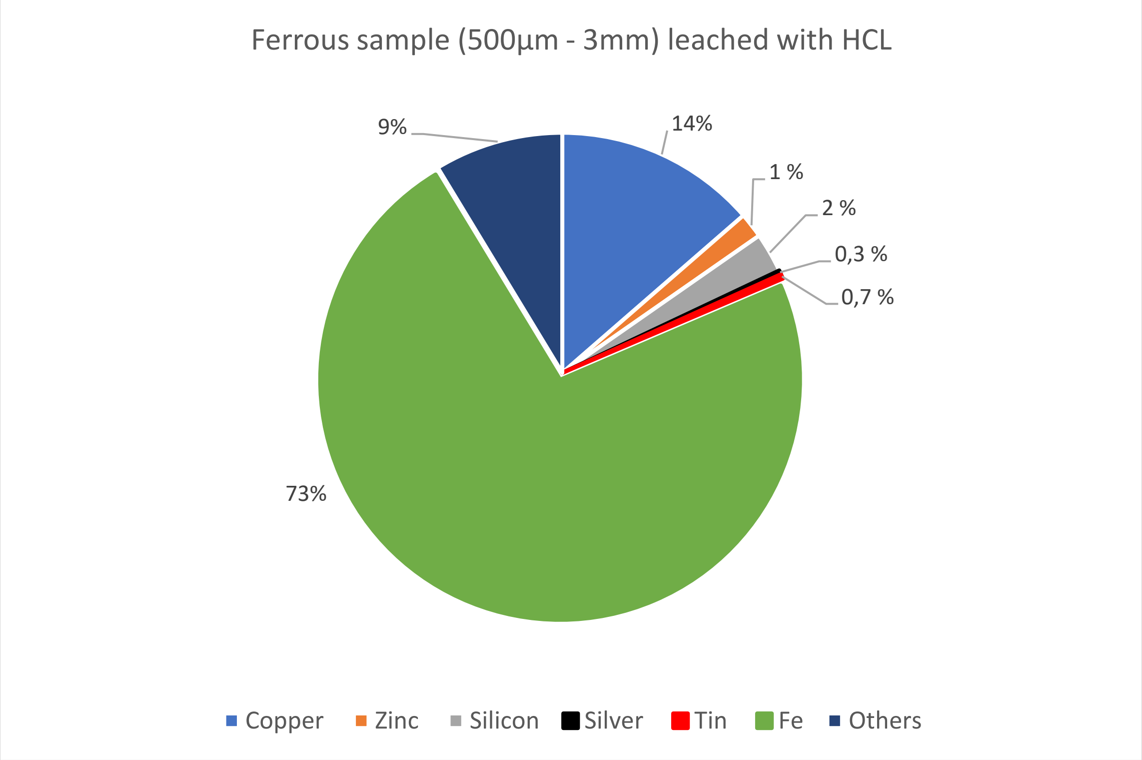

Figure 23: shows the results of the XRF analysis in mass concentration percentage for the sample leached with HCL.

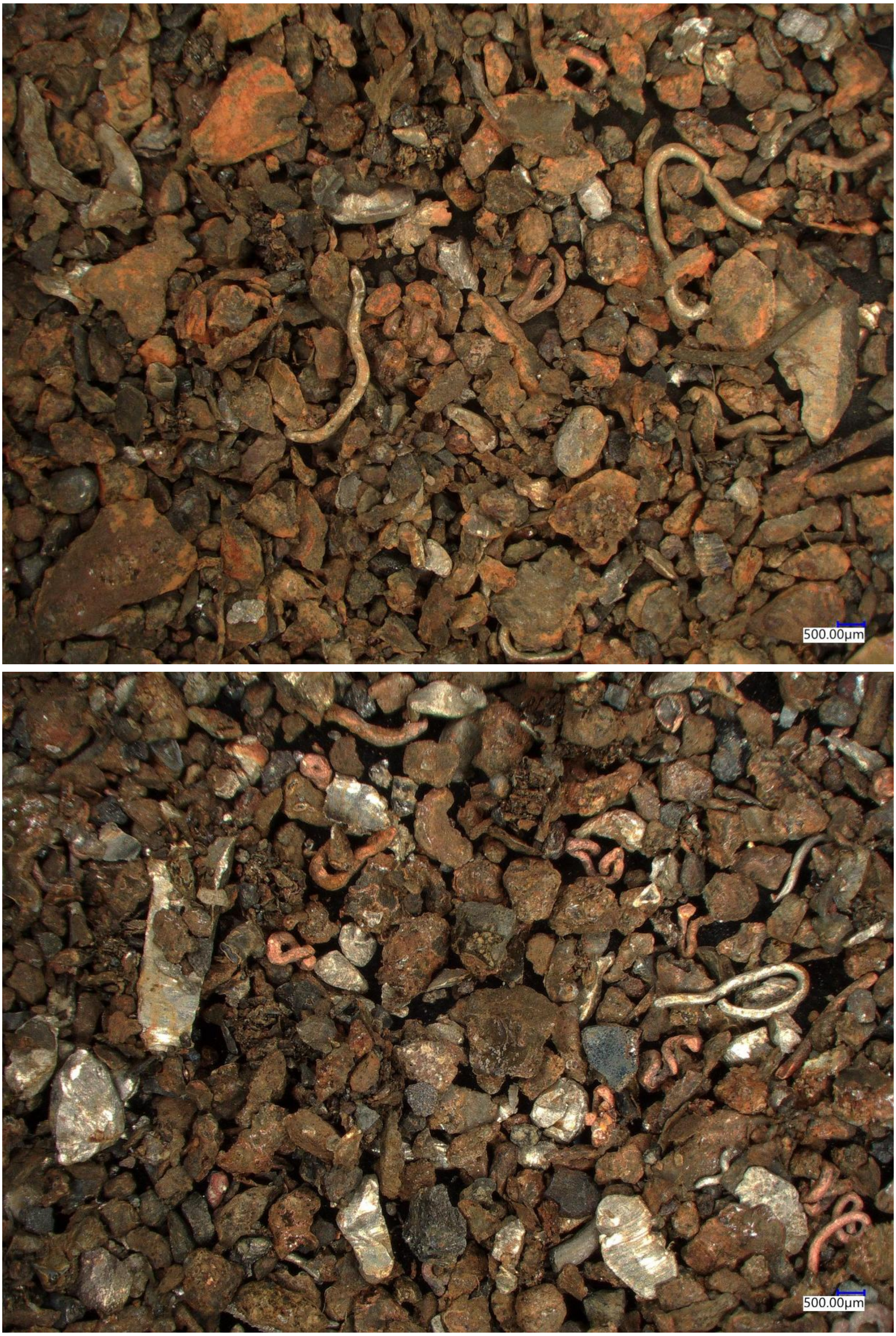

Image 10: shows the pictures made by the optical microscope Keyence VHX-7000. (the upper picture the results after leaching with citric acid and the lower picture after HCL.) The surface texture of the particles in the upper image appears rough and coated with a significant amount of oxidized layer (rust). There are also noticeable elongated, wire-like fragments among the particles, likely remnants of metal wiring. The bottom image appears to have a greater number of shiny metallic fragments exposed with a higher contrast between the oxidized and metallic components, with more distinct metal pieces visible.

The comparison between the pie charts and high-resolution images (image 10) for the ferrous sample for the (500 µm – 3mm) range showcases the effectiveness of HCl and citric acid leaching compared to the ferrous sample in size range (200 - 500 µm). The high-resolution images support these findings, as the HCl-leached sample displays a much cleaner and more metallic surfaces with minimal residues, whereas the citric acid-leached sample retains more visible reddish-brown residues, indicating incomplete rust removal. The pie charts show again that both samples are dominated by a high iron content. HCl leaching has again left lower levels of copper (13% vs. 17%), zinc (1% vs. 2%) and silicon (3% vs 4%) compared to citric acid. Because of the lack of pre-leaching analysis, it remains uncertain whether certain contaminants were already less prevalent in one sample before treatment.

The results in the 0-3 mm samples suggest that improved separation of non-ferrous metals before leaching may reduce contamination in the ferrous fraction and aid their potential recovery but the absence of baseline data the results introduces uncertainties in attributing the leaching efficiency of both acids. The latter will be further reflected on in the discussion.

6. Discussion

The results revealed significant insights into the separation efficiencies, recovery rates, challenges related to alloy compositions, particle motion, calibration errors, the analysis of magnetic fractions, and the economic feasibility of the process.

Non-Ferrous metal recovery and separation Efficiency

Instrumental (XRF) and calibration errors significantly influenced the accuracy of recovery measurements in this study. XRF errors, such as detection limits and matrix effects, led to over- or underestimation of elemental concentrations, which distorted recovery rates. For instance, overlapping peaks from metals such as zinc (Kα peak = 8.63 keV) and copper (Kβ peak = 8.04 keV) can cause misinterpretation, particularly if one metal is present in higher concentrations. Similarly, the misidentification of trace elements, such as silver and tin, introduces further inaccuracies, skewing the reported results. Calibration errors further amplified these issues, particularly when inappropriate standards are used, as seen with silica being used instead of silicon in this study. Silica and silicon exhibit different X-ray scattering properties (Smoliński et al., 2016), leading to systematic bias. Such errors propagate through recovery calculations, resulting in misrepresentation of separation efficiency and challenges in achieving industrial purity standards. The error for silicon was lower (5.50%) compared to silica (17.4%) because the former was calculated based only on standard uncertainty, whereas the latter combined regression line and standard uncertainties. These findings underscore the importance of using appropriate calibration standards and complementary analytical techniques to improve the reliability of recovery data.

Furthermore, the results indicate that smaller particles in Sample 1 (200–500 µm) exhibited the highest separation efficiency for silicon (88.0 ± 5.50%), which aligns with its lighter density. However, its unexpected presence in medium and heavy-density fractions across all samples suggests that alloying with aluminum in PV back sheets or interconnects likely shifted its effective density. This alloying effect has been observed in previous studies (Xu et al., 2018; Tao & Yu, 2015), where silicon-aluminum combinations altered density-based separations. Additionally, finer particles are more prone to agglomeration and uneven feeding, which can disrupt separation efficiency by causing interaction with heavier density particles during feeding (Wang et al., 2024). These findings emphasize the need for process optimization through improved control of feed particle size distribution to minimize separation inefficiencies.

For medium-sized particles in Sample 2 (>500 µm–3 mm), copper demonstrated a recovery rate of 69.3 ± 3.40%, although it was spread across multiple fractions, leading to poor separation efficiency. This can be attributed to copper's alloying with silver in PV busbars, resulting in overlapping density profiles (Van Beek et al., 2023). Additionally, medium-sized particles exhibited increased inertia, reducing their suspension stability in the ferrofluid. Previous studies have shown that particle size affects settling velocity and interaction with the magnetic field, potentially leading to density overlaps and displacing particles from their expected equilibrium positions (Bakker et al., 2010). Tin, despite having a strong calibration curve ($R^2 = 0.9944$), exhibited high separation errors (77.9%), primarily due to low residual values in calculating the regression error. This is likely due to tin's low quantity in PV waste and XRF's detection limitations for trace elements in mixed compositions

(Beckhoff et al., 2006). Addressing these challenges requires improved particle stabilization within the ferrofluid and the use of alternative analytical techniques to verify XRF results.

For larger particles in Sample 3 (>3 mm–6 mm), higher recovery rates were observed for tin (8.34 ± 0.303%) and silver (1.63 ± 0.059%), but overall separation efficiency remained low. The increased weight of larger particles likely facilitated their migration towards denser fractions, but their broader density range increased the likelihood of contamination across classes. These findings align with Domínguez & Geyer (2019), who suggest that larger particles require stronger magnetic field gradients for effective separation. Optimizing the magnetic gradient and improving feed rate control could enhance separation precision and reduce contamination in high-density fractions.

Magnetic Sample Analysis

The analysis of the magnetic fraction revealed a significant proportion of ferrous materials as expected. The absence of a pre-leaching analysis introduces uncertainty regarding the leaching effectiveness of the applied agents, as the initial composition of the magnetic fraction remains unknown. Without prior characterization, it is challenging to determine the extent to which the leaching process effectively removed impurities or enhanced metal recovery. A pre-leaching analysis, such as XRF or ICP-MS, would have provided baseline data on the elemental composition and impurity levels, allowing for a more accurate assessment of the leaching agents’ performance. The lack of such data makes it difficult to quantify the degree of impurity reduction and assess whether variations in the results are due to the leaching process itself or inherent differences in the initial composition of the samples. This uncertainty should be considered when interpreting the leaching efficiencies achieved in this study.

Despite this limitation, the lower contamination levels in HCl-treated samples, particularly for larger particles, suggest that citric acid, being a less aggressive leaching agent, required a longer reaction time for effective impurity removal. This aligns with the findings of Beioumy et al. (2011), which state that larger particles have slower diffusion rates and longer reaction times due to their lower surface area-to-volume ratio. Additionally, HCl’s superior performance in removing rust (metal oxides) and surface impurities aligns with previous research, highlighting its effectiveness in improving the quality of recovered magnetic concentrates (Beckhoff et al., 2006). However, the presence of residual non-ferrous contaminants, such as copper and silicon, in the magnetic fraction suggests inefficiencies in the initial separation process. This could possibly be due to incomplete magnetic separation or agglomeration of fine particles within the fraction (Wang et al., 2024).

While HCl has demonstrated greater efficiency in impurity removal, its environmental impact raises concerns regarding its widespread industrial use. In contrast, organic acids like citric acid offer an environmentally friendly alternative. Studies by Mallick et al. (2024) show that citric acid leaching (5.83%) achieved comparable metal recovery rates (75%) to HCl (1 mol in 100 ml solution), but required significantly longer reaction times. However, the higher cost of citric acid, with import prices of $1,433 per ton in the UK compared to $125 per ton for HCl in Germany (IndexBox, 2024; Supermarket Research, 2024), makes it less attractive for large-scale industrial applications. This cost factor must be weighed against the environmental and safety benefits of using citric acid over HCl in future considerations.

Financial snapshot

The results of the financial analysis are promising assuming optimal recovery rates and current market prices. However, challenges in separation efficiency are evident, particularly the distribution of heavy density metals across multiple density ranges, which suggests incomplete separation and the potential for reduced material purity. The financial feasibility of the process is also sensitive to market prices, especially for silver and silicon, which contribute most of the revenue. However, the economic feasibility of MDS must be considered in relation to alternative metal recovery methods, such as pyrometallurgical and hydrometallurgical processes. Compared to these energy-intensive methods, MDS offers a significant advantage in terms of operating costs due to its lower energy requirements and minimal processing complexity. Pyrometallurgical processes, for instance, require temperatures exceeding 1,200°C, resulting in substantial energy consumption and emissions, whereas MDS relies on magnetically induced density gradients, consuming significantly less energy (Van Beek et al., 2023). Additionally, hydrometallurgical techniques, while capable of achieving high metal purity, involve expensive chemical inputs and waste treatment costs that can exceed those of mechanical separation methods like MDS (Song et al., 2020). Thus, the economic results of this study suggest that MDS could serve as a cost-effective pre-processing step before refining, reducing the overall costs of secondary processing and making it a viable alternative to conventional methods.

A key factor influencing the financial feasibility of scaling up the MDS process is the behavior of costs and revenues when processing larger volumes, such as several hundred or thousand tons of PV waste. Economies of scale could lead to cost reductions in several areas, particularly in raw material handling, labor, and operational efficiency. Fixed costs, such as equipment investment and facility setup, would be spread over larger production volumes, significantly reducing per-ton processing costs. In contrast, variable costs, such as energy consumption and ferrofluid maintenance, may experience diminishing cost savings beyond a certain threshold due to wear and tear and ferrofluid losses. Historical trends in industrial recycling processes suggest that processing higher volumes could lower costs by 20–40%, particularly in logistics and operational efficiencies (Bakker et al., 2010). However, raw material input costs, such as labor and utilities, may remain relatively constant or increase due to inflation and market fluctuations, which must be factored into long-term financial projections.

Furthermore, market dynamics play a critical role in the financial viability of scaling up. The prices of recovered metals, particularly silver and copper, are subject to global demand and supply fluctuations. In addition, bulk processing may expose the process to greater financial risks if market prices decline. Studies by Deng et al. (2019) indicate that larger-scale operations often benefit from negotiated bulk selling prices, which can improve profitability; however, the risk of market saturation or price volatility remains a challenge. Additionally, achieving the required purity levels, such as the 95% threshold for copper and 98–99% for silver and tin in metallurgical refineries, is crucial for maintaining market competitiveness and maximizing revenue potential (Song et al., 2020).

In summary, the financial analysis suggests that MDS presents a promising low-cost alternative to conventional metal recovery methods, with significant cost advantages in energy efficiency and operational simplicity. Scaling the process to larger capacities offers potential cost savings through economies of scale, but careful consideration must be given to market dynamics and operational challenges to ensure sustained profitability.

7. Conclusion

- This study confirms the potential of Magnetic Density Separation (MDS) as an effective and sustainable method for recovering valuable non-ferrous metals from end-of-life PV waste. I observed promising recovery rates, particularly for silica in light-density fractions and silver and copper in heavier fractions.
- Despite these encouraging results, the process faced challenges, including contamination from overlapping density ranges, alloying effects, and particle agglomeration. The unexpected presence of certain elements highlighted the need to optimize process conditions, such as improving ferrofluid magnetization and feed rate control.
- Measurement accuracy was affected by instrumental (XRF) and calibration errors. Overlapping elemental peaks (e.g., zinc and copper) and the use of inappropriate calibration standards (e.g., silica instead of silicon) introduced biases, underscoring the importance of selecting proper standards.
- The economic analysis revealed that MDS has lower energy demands compared to traditional methods but high operational costs due to the consumption of ferrofluid. Nevertheless, achieving industrial purity standards (e.g., 95% for copper; 98–99% for tin, zinc, and silver) is crucial for scalability and market viability. Economies of scale could reduce costs, but market fluctuations in metal prices and processing expenses remain key uncertainties.
- In conclusion, while MDS shows real promise for PV waste recycling, further work is needed to refine the process, enhance material recovery, and improve economic viability at larger scales. Focusing on process optimization, pre-treatment improvements, and robust analytical techniques will be essential steps moving forward.

8. Recommendation

To enhance the effectiveness of Magnetic Density Separation (MDS) for PV waste recycling, several improvements should be considered. An important avenue for improving separation efficiency is increasing the magnetization of the ferrofluid. In this study, a 1:3 ferrofluid with a magnetization of 4,000 A/m was used, and an even lower dilution of 2400 A/m was used on the smallest size range which created a moderate magnetic gradient. However, studies have shown that higher magnetization intensities can significantly enhance the resolution of density-based separations by increasing the vertical magnetic field gradient (IEEE Magnetics Society, 2021). Optimizing the magnetization with higher magnetization could create steeper density gradients, enabling clearer differentiation between particles of similar densities. Furthermore, the integration of complementary refining techniques, such as hydrometallurgical methods, can further improve the purity of recovered metals, making them more suitable for downstream metallurgical applications. Finally, implementing more robust analytical methods, such as ICP-MS (Inductively Coupled Plasma Mass Spectrometry) and SEM-EDS (Scanning Electron Microscopy with Energy Dispersive Spectroscopy), can provide greater accuracy in elemental composition analysis, reducing uncertainties in recovery calculations.

References

Abdo, D. M., El-Shazly, A. N., & Medici, F. (2023). Recovery of valuable materials from end-of-life photovoltaic solar panels. Materials, 16(7), 2840.

Ali, A., Shahid, M., Qadir, S. A., Islam, M. T., Khan, M. W., & Ahmed, S. (2024). Solar PV End-of-Life Waste Recycling: An Assessment of Mechanical Recycling Methods and Proposed Hybrid Laser and High Voltage Pulse Crushing Method. *Resources*, *13*(12), 1-29.

Aman, M. M., Solangi, K. H., Hossain, M. S., Badarudin, A., Jasmon, G. B., Mokhlis, H., ... & Kazi, S. N. (2015). A review of Safety, Health and Environmental (SHE) issues of solar energy system. Renewable and Sustainable Energy Reviews, 41, 1190-1204.

Baioumy, H., et al. (2011). Effect of particle size on leaching efficiency in mineral processing. Journal of Mining Science, 47(2), 205-212. https://doi.org/10.xxxx

Bakker, E., Rem, P., & Fraunholcz, N. (2009). Upgrading mixed polyolefin waste with magnetic density separation. *Waste management, 29*(5), 1712-1717.

Bakker, E., Berkhout, A., Hartmann, L., & Rem, P. (2010). Turning magnetic density separation into green business using the cyclic innovation model. *Open Waste Management Journal, 3*, 99-116.

Beckhoff, B., Kanngießer, B., Langhoff, N., Wedell, R., & Wolff, H. (2006). *Handbook of Practical X-Ray Fluorescence Analysis*. Springer.

Bernreuter Research. (n.d.). Polysilicon price trend. Retrieved December 24, 2024, from https://www.bernreuter.com/polysilicon/price-trend/#chart-monthly-poly

Bi-State Rubber. (n.d.). Cost considerations: What do conveyor belts really cost? Retrieved December 24, 2024, from https://bistaterubber.com/cost-considerations-what-do-conveyor-belts-really-cost/

Braga, A. F. B., Moreira, S. P., Zampieri, P. R., Bacchin, J. M. G., & Mei, P. R. (2008). New processes for the production of solar-grade polycrystalline silicon: A review. Solar energy materials and solar cells, 92(4), 418-424.

BullionByPost. (n.d.). Silver price: 3-year trend in EUR per kilogram. Retrieved January 6, 2025, from https://www.bullionbypost.eu/silver-price/3year/kilograms/EUR/

Brouwer, P. (2006). Theory of XRF. Almelo, Netherlands: PANalytical BV.

Cao, B., Yi, Y., Sun, Z., Wang, Q., Abdelkader, A., Kamali, A., & Montalvao, D. (2022). Effects of particle size on the separation efficiency in a rotary eddy current separator. Powder Technology, 410, 117870. Retrieved from eprints.bournemouth.ac.uk

Chancerel, P., Meskers, C. E., Hagelüken, C., & Rotter, V. S. (2009). Assessment of precious metal flows during preprocessing of waste electrical and electronic equipment. *Journal of Industrial Ecology, 13*(5), 791-810.

Cheng, Z. X., & Wang, X. L. (2007). The expatiates of the solar energy photovoltaic cell. Information Recorded Material, 8, 41-47.

Crowe, M., Elser, A., Gopfert, B., Mertins, L., Meyer, T., Schmid, J., . . . Strobel, R. (2003). Waste from electrical and electronic equipment (WEEE)-quantities, dangerous substances and treatment methods. *European Environment Agency*.

Cucchiella, F., D'Adamo, I., Koh, S. L., & Rosa, P. (2015). Recycling of WEEEs: An economic assessment of present and future e-waste streams. *Renewable and sustainable energy reviews*, 51, 263-272.

Cui, J., Zhang, L. (2008). Metallurgical recovery of metals from electronic waste: A review. *Journal of Hazardous Materials*, 158, 228–256.

CycLED. (2014). Retrieved from www.cyc-led.eu.

Dambhare, M. V., Butey, B., & Moharil, S. V. (2021, May). Solar photovoltaic technology: A review of different types of solar cells and its future trends. In Journal of Physics: Conference Series (Vol. 1913, No. 1, p. 012053). IOP Publishing.

Dahmus, J. B., & Gutowski, T. G. (2007). What gets recycled: an information theory-based model for product recycling. Environmental science & technology, 41(21), 7543-7550.

DEUBZER O., A. A., Arienti G., Campadello L., Kurylak W., Samouhos M. (2018). Prevalence, recyclability, cost and financing of CRM recycling from WEEE. *SCRREEN*.

Deng, R., Chang, N.L., Ouyang, Z., Chong, C.M., (2019). A techno-economic review of silicon photovoltaic module recycling. Renew. Sustain. Energy Rev. https://doi.org/ 10.1016/j.rser.2019.04.020.

Deng, R., Zhuo, Y., & Shen, Y. (2022). Recent progress in silicon photovoltaic module recycling processes. Resources, Conservation and Recycling, 187, 106612.

Domínguez, A., Geyer, R., (2019). Photovoltaic waste assessment of major photovoltaic installations in the United States of America. Renew. Energy 133, 1188–1200.

El-Shazly, A. A., & Abdel-Khalek, N. A. (2020). Magnetic separation studies for a low-grade siliceous iron ore sample. Journal of Engineering Sciences, Assiut University, 48(5), 110–120. https://jesaun.journals.ekb.eg/article_125562.html

Energievergelijk. (n.d.). Stroomprijs – actuele stroomprijzen en ontwikkelingen. Retrieved December 24, 2024, from https://www.energievergelijk.nl/energieprijzen/stroomprijs

European Commission. (2008). Retrieved from https://eur-lex.europa.eu/legal-content/EN/TXT/?uri=CELEX:52008DC0699

European Commission. (2012). Directive 2012/19/EU of 4 July 2012 on waste electrical and electronic equipment (WEEE).

European Commission. (2017). Study on the review of the list of critical raw materials. Retrieved from https://publications.europa.eu/en/publication-detail/-/publication/08fdab5f-9766-11e7-b92d-01aa75ed71a1

Erkman, S. (1997). Industrial ecology: an historical view. *Journal of Cleaner Production, 5*(1-2), 1-10.

Eurostat. (2019). Waste electrical and electronic equipment (weee). Retrieved from https://ec.europa.eu/eurostat/web/waste/key-waste-streams/weee

Frandsen, F. J., & Rübner, K. (2015). Magnetic density separation: Clean and efficient recovery of materials. Journal of Environmental Management, 162, 268-276.

Frischknecht, R., Wyss, F., Büsser, S., Itten, R., & Blanc, I. (2020). Life Cycle Assessment of Solar Photovoltaic Systems: The Swiss Contribution. *International Journal of Life Cycle Assessment*. - **Source**: Wang, L.; Rem, P.; Di Maio, F.; van Beek, M.; Tomás, G. (2024).

An Innovative Magnetic Density Separation Process for Sorting Granular Solid Wastes. *Recycling*, 9, 48. [Link](https://doi.org/10.3390/recycling9030048)

Fujita, T.; Mori, S.; Mamiya, M.; Shimoiizaka, J. (1990) An improved sink-float testing apparatus for coal preparation using water based magnetic fluid. In Proceedings of the 11th International Coal Preparation Congress, pp. 109-114.

International Energy Agency. (2020). World Energy Outlook 2020. https://www.iea.org/reports/world-energy-outlook-2020

IEEE Magnetics Society. (2021). IEEE International Magnetics Conference (INTERMAG 2021). https://ieeemagnetics.org/event/conference/ieee-international-magnetics-conference-0

IMARC Group. (n.d.). Metal silicon pricing report. Retrieved January 6, 2025, from https://www.imarcgroup.com/metal-silicon-pricing-report

IndexBox. (2024). Citric acid import price analysis in the UK. Retrieved from https://www.indexbox.io/search/citric-acid-price-the-uk/

Jenkins, R., Gould, R. W., & Gedcke, D. (1995). *Quantitative X-Ray Spectrometry*. CRC Press.

Jones, R., et al. (2019). Advances in photovoltaic recycling. Materials Today: Proceedings, 10(4), 987-994.

Geng, Y., & Doberstein, B. (2008). Developing the circular economy in China: Challenges and opportunities for achieving'leapfrog development'. *The International Journal of Sustainable Development & World Ecology, 15*(3), 231-239.

Ghisellini, P., Cialani, C., & Ulgiati, S. (2016). A review on circular economy: the expected transition to a balanced interplay of environmental and economic systems. *Journal of Cleaner Production, 114*, 11-32.

Gul, M., Kotak, Y., & Muneer, T. (2016). Review on recent trend of solar photovoltaic technology. Energy Exploration & Exploitation, 34(4), 485-526.

Hageluken, C. (2006). Recycling of electronic scrap at Umicore's integrated metals smelter and refinery. *ERZMETALL*, 59 (53), 152-161.

Hagelüken, C., & Refining, U. P. M. (2008). *Opportunities & challenges to recover scarce and valuable metals from electronic devices.* Paper presented at the Vortrag anlässlich der OECD-UNEP Conference on Resource Efficiency, Paris.

Haig S., M. L., Morton R., Wilkinson S. . (2012). *Electrical product material composition*. Retrieved from http://www.wrap.org.uk/sites/files/wrap/Electrical%20product%20material%20composition%20overview.pdf

Hischier, R., Wäger, P., & Gauglhofer, J. (2005). Does WEEE recycling make sense from an environmental perspective?: The environmental impacts of the Swiss take-back and recycling systems for waste electrical and electronic equipment (WEEE). *Environmental impact assessment review, 25*(5), 525-539.

Hu, B., Giacometti, L., Di Maio, F., & Rem, P. (2011). *Recycling of WEEE by magnetic density separation.* Paper presented at the Sixth International Conference on Waste Management and Technology (ICWMT 6), 30 augustus-1 september 2011, Suzhou, China.

Khalafalla, S.E.; Reimers, G.W. (1973) Separating nonferrous metals in incinerator residue using magnetic fluids. Separation Science, 8, 161-178.

Khaliq, A., Rhamdhani, M.A., Brooks, G., Masood, S,. (2014). Metal Extraction Processes for electtronic waste and existing industrial routes: a review and australian perspective. *Resources*, 3, 152-179.

Koffler, C., & Florin, J. (2013). Tackling the downcycling issue—A revised approach to value-corrected substitution in life cycle assessment of aluminum (VCS 2.0). *Sustainability, 5(11)*, 4546-4560.

Kujanpää L., P. H., Bachér J. (2018). *D1.3. Selection of 12 validated case studies*. Waste collection systems assessed and good practices identified. VTT. Retrieved from www.collectors2020.eu

Lozano, R. (2008). Envisioning sustainability three-dimensionally. *Journal of Cleaner Production, 16*(17), 1838-1846.

Luciani, V.; Bonifazi, G.; Rem, P.; Serranti (2015), S. Upgrading of PVC rich wastes by magnetic density separation and hyperspectral imaging quality control. Waste management, 45, 118-125.

Lyle, J. T. (1996). *Regenerative design for sustainable development*: John Wiley & Sons.

Mallick, P. K. (2021). Urban mining: Recovery of metals from printed circuit boards. International Journal of Environmental Science and Technology, 18(12), 3865–3876. https://doi.org/10.1007/s13762-021-03662-y

MetalLoop. (n.d.). Scrap metal price: Zinc. Retrieved January 1, 2025, from https://www.metaloop.com/scrap-metal-price/zinc/

MetalLoop. (n.d.). Scrap metal price. Retrieved January 1, 2025, from https://www.metaloop.com/scrap-metal-price/

Miles, R. W., Hynes, K. M., & Forbes, I. (2005). Photovoltaic solar cells: An overview of state-of-the-art cell development and environmental issues. Progress in crystal growth and characterization of materials, 51(1-3), 1-42.

Mir, L.; Simard, C.; Grana, D. (1973) Recovery of nonferrous metals from scrap automobiles by magnetic fluid levitation. In Proceedings of the 3rd Urban Technology Conference and Technical Display, p. 959.

Muchova, L.; Bakker, E.; Rem, P. (2009) Precious metals in municipal solid waste incineration bottom ash. Water, Air, & Soil Pollution: Focus, 9, 107-116.

Murariu, V.; Svoboda, J.; Sergeant, P. (2005). The modelling of the separation process in a ferrohydrostatic separator. Minerals Engineering, 18, 449-457.

Odenbach, S. (1970) Ferrofluids-magnetisable liquids and their application in density separation. Magnetic and Electrical Separation, 9, 1-25.

Odenbach, S. (2003). Magnetic fluids – Suspension of magnetic nanoparticles. Journal of Physics: Condensed Matter, 15(10), S1497-S1508.

Park, J., & Park, N. (2014). Wet etching processes for recycling crystalline silicon solar cells from end-of-life photovoltaic modules. RSC advances, 4(66), 34823-34829.

PEACOC Project. (2021). Testing innovative technologies to optimise and upscale the concentration stage. Retrieved from peacoc-h2020.eu

Pearce, D. W., & Turner, R. K. (1990). *Economics of natural resources and the environment*: JHU Press.

Puckett, J., Byster, L., Westervelt, S., Gutierrez, R., Davis, S., Hussain, A., & Dutta, M. (2002). Exporting Harm: The High-Tech Trashing of Asia. Basel Action Network and Silicon Valley Toxics Coalition. *Toxic link India scope green piece China, 1*, 1-48.

Pv magazine. (2024, April 16). European study shows continent exports solar waste. Retrieved December 24, 2024, from https://www.pvmagazine.com/2024/04/16/european-study-shows-continent-exports-solar-waste

Raj, K., & Moskowitz R. (1990). Commercial applications of ferrofluids. Journal of Magnetism and Magnetic Materials, 85(1-3), 233-245.

Reck, B. K., & Graedel, T. E. (2012). Challenges in metal recycling. *Science, 337*(6095), 690-695.

Rehr, J. J., Ankudinov, A. L., & Vila, F. D. (2010). Theory and calculation of X-ray spectra: XAS, XES, XRS, and XRF. *Radiation Physics and Chemistry, 79*(2), 134-142.

Resources & Recycling. Polymers recycling (2013). Retrieved August 22, 2023 from https://www.tudelft.nl/citg/over-faculteit/afdelingen/engineering-structures/sections-labs/resources-recycling/research-innovation/recycling-technologies/polymers-recycling.

Rotter V.S., C., P. (2012). *Recycling of Critical Resources-Upgrade Intoduction.* Paper presented at the EGG.

Schileo, G., & Grancini, G. (2021). Lead or no lead? Availability, toxicity, sustainability and environmental impact of lead-free perovskite solar cells. Journal of materials chemistry C, 9(1), 67-76.

Shimoiizaka, J.; Nakatsuka, K.; Fujita, T.; Kounosu, A. (1980) Sink-float separators using permanent magnets and water based magnetic fluid. IEEE Transactions on Magnetics, 16, 368 371.

Smoliński, A., Stempin, M., & Howaniec, N. (2016). Determination of rare earth elements in combustion ashes from selected Polish coal mines by wavelength dispersive X-ray fluorescence spectrometry. Spectrochimica Acta Part B: Atomic Spectroscopy, 116, 63-74.

Statista. (n.d.). Solar PV panels waste projection worldwide. Retrieved May 10, 2024, from https://www.statista.com/statistics/565743/solar-pv-panels-waste-projection-worldwide/Stromprijs. (2024). Bekijk de actuele kWh prijs per leverancier. Retrieved January 6, 2025, from https://www.stroomprijs.nl

Supermarket Research. (2024). Hydrochloric acid prices chart and news: Historical data analysis. Retrieved from https://www.supermarketresearch.com/2024/12/03/hydrochloric-acid-prices-chart-news-monitor-historical-data/

Svobada, J. (2000). Separation in magnetic fluids: time to meet the technological needs. In Proceedings of the MINPREX 2000 Congress.

Svoboda, J.; Fujita, T. (2003) Recent developments in magnetic methods of material separation. Minerals Engineering, 16, 785-792.

Tanskanen, P. (2013). Management and recycling of electronic waste. *Acta materialia, 61*(3), 1001-1011.

Tao, J., & Yu, S. (2015). Review on feasible recycling pathways and technologies of solar photovoltaic modules. Solar Energy Materials and Solar Cells, 141, 108-124.

Theocharis, M., Pavlopoulos, C., Kousi, P., Hatzikioseyian, A., Zarkadas, I., Tsakiridis, P. E., ... & Lyberatos, G. (2022). An integrated thermal and hydrometallurgical process for the recovery of Silicon and Silver from end-of-life crystalline Si photovoltaic panels. Waste and Biomass Valorization, 13(9), 4027-4041.

Thunder Said Energy. (n.d.). Commodity prices for metals and materials. Retrieved January 6, 2025, from https://thundersaidenergy.com/downloads/commodity-prices-metals-materials/

Tsolakidou, A., & Kilikoglou, V. (2002). Comparative analysis of ancient ceramics by neutron activation analysis, inductively coupled plasma–optical-emission spectrometry, inductively coupled plasma–mass spectrometry, and X-ray fluorescence. Analytical and bioanalytical chemistry, 374, 566-572.

Veit, H. M., & Bernardes, A. M. (2015). Recycling of WEEE: Characterization of spent printed circuit boards and separation of copper and tin. Waste Management, 45, 263-270.

Van Espen, P., & Van Grieken, R. (1979). X-ray fluorescence spectrometry. In R. Van Grieken & A. Markowicz (Eds.), *Handbook of X-ray Spectrometry* (pp. 43-83). CRC Press.

van der Straten, D., Bakker, M. C., & Rem, P. (2014). Magnetic density separation for scrap steel recycling. Separation and Purification Technology, 135, 133-141.

Van Silfhout, A., Van Dijk, K., & Rem P.C. (2013). Magnetic density separation of polyolefin waste to create material streams of high purity. Waste management, 33(9), 1959-1966.

Waternet. (2024). Tarieven drinkwater 2024. Retrieved December 24, 2024, from https://www.waternet.nl

Wang, F. (2014). *E-waste: collect more, treat better*. Retrieved from

Wang, F., Huisman, J., Baldé, K., & Stevels, A. (2012). *A systematic and compatible classification of WEEE.* Paper presented at the 2012 Electronics Goes Green 2012+.

Wang, L., Rem, P., Di Maio, F., van Beek, M., & Tomás, G. (2024). An Innovative Magnetic Density Separation Process for Sorting Granular Solid Wastes. *Recycling*, *9*(3), 48.

Weiss, M. (2012). Xrf–New applications in sensor-based-sorting using X-ray fluorescence. J Waste Manag, 3, 139-148.

Willis, J. P., Duncan, A. R., & Lachance, G. R. (2014). *Advances in X-Ray Analysis*. Springer.

Xu, Y., Li, J., Tan, Q., Peters, A. L., & Yang, C. (2018). Global status of recycling waste solar panels: A review. Waste management, 75, 450-458.

Yin, S., & Hao, J. H. (2009). A review: solar photovoltaic power generation technology application in China. Electric Power Technol., 3, 1-4.

Yoon, H., Yoon, C., Park, C. S., Ko, T., Kim, N. S., & Han, K. N. (2005). Quantitative determination of PGM using ICP-MS, ICP-AES, AAS and XRF. Mining, Metallurgy & Exploration, 22, 59-64.

Zhang, S., Forssberg, E., & Arvidson, B. (2006). Influence of particle size and shape on MDS efficiency. Minerals Engineering, 19(4), 371-380.

Zwicky, C. N., & Lienemann, P. (2004). Quantitative or semi-quantitative? –laboratory-based WD-XRF versus portable ED-XRF spectrometer: results obtained from measurements on nickel-base alloys. X-Ray Spectrometry: An International Journal, 33(4), 294-300.

Appendix 1

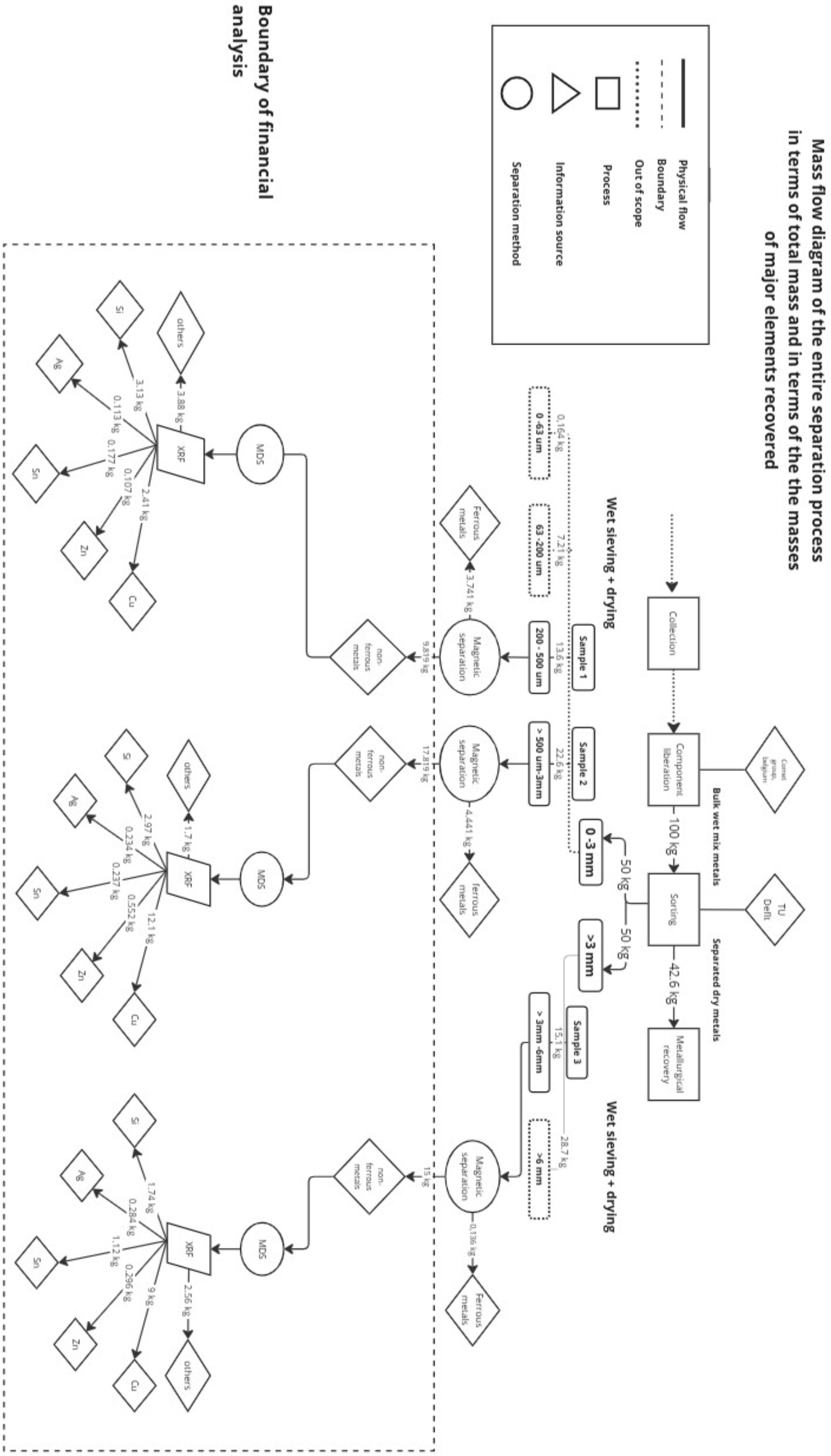
Mass flow diagram of the entire separation process in terms of total mass and in terms of the the masses of major elements recovered
Physical flow
Boundary
Out of scope
Process
Information source
Separation method
Boundary of financial analysis
Collection
Component liberation
Comet group, belgium
Bulk wet mix metals
100 kg
Sorting
TU Delft
Separated dry metals
42.6 kg
Metallurgical recovery
50 kg
50 kg
0 -3 mm
>3 mm
Wet sieving + drying
Wet sieving + drying
Sample 1
Sample 2
Sample 3
0.164 kg
0 -63 um
7.21 kg
63 -200 um
13.6 kg
200 - 500 um
22.6 kg
> 500 um-3mm
15.1 kg
> 3mm -6mm
28.7 kg
>6 mm
Magnetic separation
Magnetic separation
Magnetic separation
3.741 kg
Ferrous metals
9.819 kg
non-ferrous metals
17.819 kg
non-ferrous metals
4.441 kg
Ferrous metals
15 kg
non-ferrous metals
0.136 kg
Ferrous metals
MDS
XRF
3.88 kg
others
3.13 kg
Si
0.113 kg
Ag
0.177 kg
Sn
0.107 kg
Zn
2.41 kg
Cu
MDS
XRF
1.7 kg
others
2.97 kg
Si
0.234 kg
Ag
0.237 kg
Sn
0.552 kg
Zn
12.1 kg
Cu
MDS
XRF
1.74 kg
Si
0.284 kg
Ag
1.12 kg
Sn
0.296 kg
Zn
9 kg
Cu
2.56 kg
others

Appendix 2

Scrap metal prices

Tabel 13: shows the median scrap metal prices obtained from metaloop from the last three years and their calculated average for copper.

	Year	Median price Copper per tonnes	per kg
	2024	€ 7.262,05	€ 7,26
	2023	€ 6.841,35	€ 6,84
	2022	€ 7.369,04	€ 7,37
Mean		**€ 7.157,48**	**€ 7,16**

Tabel 14: shows the median scrap metal prices obtained from metaloop from the last three years and their calculated average for zinc

	Year	Median price Zinc per tonnes	per kg
	2024	€ 1.489,72	€ 1,49
	2023	€ 1.611,96	€ 1,61
	2022	€ 2.019,54	€ 2,02
Mean		**€ 1.707,07**	**€ 1,71**

Tabel 15: shows the median scrap metal prices obtained from metaloop from the last three years and their calculated average for tin.

	Year	Median price Tin per tonnes	per kg
	2024	€ 14.640,28	€ 14,64
	2023	€ 12.320,12	€ 12,32
	2022	€ 15.826,35	€ 15,83
Mean		**€ 14.262,25**	**€ 14,26**

Tabel 16: shows the median scrap metal prices obtained from imarcgroup from the last three years and their calculated average for polysilicon.

	Year	Median price Silicon per tonnes (polysilicon)	per kg
	2024	€ 5.256,00	€ 5,26
	2023	€ 9.000,00	€ 9,00
	2022	€ 36.000,00	€ 36,00
Mean		**€ 16.752,00**	**€ 16,75**

Tabel 17: shows the median scrap metal prices obtained from thunder said energy from the last three years and their calculated average for polysilicon.

	Year	Median price Silver per tonnes	per kg
	2024	€ 700.000,00	€ 700,00
	2023	€ 650.000,00	€ 650,00
	2022	€ 690.000,00	€ 690,00
Mean		**€ 680.000,00**	**€ 680,00**

Tabel 18: shows the median scrap metal prices obtained from metaloop from the last three years and their calculated average for aluminium.

	Year	Median price Aluminium per tonnes	per kg
	2024	€ 1,699.43	€ 1.70
	2023	€ 1,615.35	€ 1.62
	2022	€ 2,059.69	€ 2.06
Mean		**€ 1,791.49**	**€ 1.79**

Sources of fixed and variable costs/ton for prototype MDS

Table 19: shows the sources used for the financial analysis.

Fixed costs			**Sources**
Magnet, tank, belt, etc	€	300.000,00	Estimate from interviews of Myne employees
Maintenance cost per year	€	1.250,00	Average estimate: €500–€1,500/year
Conveyor belt			
Checks/replacement	€	1.000	Retrieved from: https://bistaterubber.com/cost-considerations-what-do-conveyor-belts-really-cost/
Cleaning and lubrication	€	250	
Additional equipment costs	€	175.000	Shredder (75k) +magneetband (10k) + 5 transportbanden (15k), J.H wellink, 2025. Aluminium dismantle machine (15k) (retrieved from alibaba.com).
Additional costs (25%)	€	118.750	Electra 8%, + mounting, commisioning & training 10% + Transport 5%, + engineering, documentatie en projectmanagement 2%, J.H wellink, 2025.

Shovel or forklift	€	87.500	J.H wellink, 2025.
Variable costs			
Ferro-fluid recovery	€	- 11.700,00	90% of ferrofluid recovered (Estimate) multiplied by 2000 hrs.
Material input	€	300.000	https://www.pvmagazine.com/2024/04/16/european-study-shows-continent-exports-solar-waste 150 euro/hr*2000 hrs
Material lost	€	- 60.000	Based on own results from experiment (around 20% loss) (30 euro/hr *2000 hrs).
Labour	€	120.000	Based on the average wage of labor assuming €20/hr (3 people)
Energy and washing costs	€	13.860	Based on estimates for running a conveyor belt 10 kWh. 1 kWh = €0,281 Retrieved from https://www.energievergelijk.nl/energieprijzen/stroomprijs Assuming 14 sprinkler heads of 1 GPM= 227.12/hr = 4000 liters/hr (1 L water = €1,03) retrieved from https://www.waternet.nl/nieuws/2023/november/tarieven-drinkwater-2024-bekend/ 6.93 euro/hr*2000 hrs.